ARMY RESEARCH LABORATORY

PILOT-81 VVA EXPERIMENT-Analysis of the Multi-Path Transmissometer-Radiometer Measurements

R.A. Sutherland and J.E. Butterfield

ARL-TR-2953 **April 2003**

NOTICES

Disclaimers

The findings in this report are not to be construed as an official Department of the Army position, unless so designated by other authorized documents.

Citation of manufacturers' or trade names does not constitute an official endorsement or approval of the use thereof.

DESTRUCTION NOTICE—When this document is no longer needed, destroy it by any method that will prevent disclosure of its contents or reconstruction of the document.

Army Research Laboratory
White Sands Missile Range, NM 88002-5513

ARL-TR-2953 **April 2003**

PILOT-81 VVA EXPERIMENT-Analysis of the Multi-Path Transmissometer-Radiometer Measurements

R.A. Sutherland and J.E. Butterfield
Survivability/Lethality Analysis Directorate, ARL

Contents

List of Figures

Tables

Preface

In modeling the effects of infrared (IR) screening smokes on battlefield operations, one must account for the fact that the obscurant itself can be a strong source of IR radiation, often generating signals comparable to, or even much greater than, those from potential targets. The degree to which this happens is dependent upon the aerosol optical thickness, emissivity, and temperature as they affect absorption, scattering, and natural blackbody (thermal) emissions, which for the conditions normally encountered in terrestrial applications, are strongest at the IR wavelengths. The problem has been recognized for some time by the user community and requirements for incorporating emissive effects into the classical wargame models such as CASTFOREM have been put forth by both the U.S. Army Training and Doctrine Command (TRADOC) and the National Ground Intelligence Center (NGIC). The problem was addressed by the U.S. Army Research Laboratory (ARL)/Survivability Lethality Analyses Directorate (SLAD) staff in the mid-1990s as part of a pilot program from which arose the creation of a formal technical program called SCIMITAR[1] which eventually led to the development of the PILOT81[2] model for simulating emissive sources and later to the execution of the field experiment of the same name described herein. All work was performed in-house through various SLAD tools, techniques, and met (TTM)] programs supported with 6.2 (development) funding and in cooperation with SLAD system leaders supported with 6.6 (analysis) funding. The major purpose of the experiment was to provide an accurate and reliable database for the development and verification of the PILOT81 model (and any others of similar capability). The main source of data was acquired with the ARL/SLAD Multiple-Path Transmissometer Radiometer System, or MPTR, which provided the measurements necessary to determine both the obscurant direct transmittance and the more illusive path emission and radiance required for modeling emissive smokes. These initial experiments were limited in scope to eight field trials and two obscurant types released into the atmosphere at temperatures slightly above ambient and thus include effects of both thermal emission and multiple in-scattering over four spectral bands from the visible through far IR.

[1] Anderson, L., Chenault, T., Churchman, J., Homack, R. and T. Smelker, 1999, "SCIMITAR-Scene and Countermeasure Integration for Munition Interaction with Targets", U.S. Army Research Laboratory Technical report, ARL-TR-1633, September 1999.

[2] Sutherland, R.A, 2002, "Determination and use of IR band Emissivities in a Multiple Scattering and Thermally Emitting Aerosol Medium", U.S. Army Research Laboratory Technical Report, ARL-TR-2688, July 2002.

Acknowledgements

The following U. S. Army Research Laboratory, Survivability/Lethality Analyses Directorate personnel participated in the field experiment: Joe Churchman, Test Conductor; Lon Anderson, infrared imagery; Steve Lacy, meteorological data; Eric Boschert and Ron Hagy, Aerosol Generator. Charlie Garret wrote the environmental impact statement and did the search of existing obscurants databases; and Felicia Chamberlain supervised the safety requirements. Charles Lopez, New Mexico Sate University student, performed the data reduction on the dual band imagery and helped with the data. Mr. Pete Schugart, Training and Doctrine Command Analysis Center /White Sands Missile Range and Mr. Frank Poleski, National Ground Intelligence Center, were the original catalysts driving the requirements for emissive smokes modeling.

Executive Summary

The PILOT81 Emissive Sources Verification Experiment produced one of the few databases available for quantifying the radiative emissions of infrared (IR) screening smokes and the potential effects on multi-band sensor systems. The major source of data was the U.S. Army Research Laboratory (ARL), Survivability/Lethality Analyses Directorate (SLAD) Multi-Path Transmissometer Radiometer (MPTR) system which provided near simultaneous and collinear measurements of both direct transmission and total radiance over three sampling paths (two transmission and one total radiance) and four spectral bands from the visible through far IR. Other on-site instrumentation included a

- dual band IR imager
- meteorological van
- high volume aerosol generator

The experiments, per se, consisted of eight trials utilizing both brass and graphite flakes as the (airborne) emissive obscurant. Obscurants were released into the atmosphere at four distinct mass flow rates producing semi-continuous aerosol clouds corresponding to a range of optical depths from $\tau=0$ to a maximum of about $\tau=8$. The formal objective of the experiment was to provide a database for developing and evaluating obscuration models used in IR scene simulations such as SCIMITAR[1]. The study also utilized the newly invented "Log-R" correlation method to enable a direct experimental determination of the "sky-to-ground" parameter which is a key input for contemporary sensor performance models and a requirement for modeling such systems in tactical wargames such as (CASTFOREM)[2]. The experiments also filled a significant void in the Army's program of "Smoke Weeks" which offers a wealth of information on aerosol transmissivity but leaves a significant dearth of information on aerosol emissivity (and reflectivity) which are key to modeling emissive aerosol effects. The primary models chosen as representative of the current state-of-the-art in Army modeling applications are COMBIC[3] for determining cloud transmittance and PILOT81[4] for determining path emission/radiance. Overall the MPTR measurements produced convincing evidence for the validity of the newly developed Log R method for analyzing path radiance as well as the more usual Log T method for analyzing transmission measurements. In general, the obscurant mass extinction coefficients determined from the MPTR transmissometer measurements agreed with COMBIC for all four spectral bands that were considered. Also the results from the MPTR

[1] Anderson, L., Chenault, T. Churchman, J., Homack, R. and T. Smelker, 1999, "SCIMITAR-Scene and Countermeasure Integration for Munition Interaction with Targets", U.S. Army Research Laboratory Technical report, ARL-TR-1633, September 1999.

[2] Mackey, D.C., Dixon, D.S., Jensen, K.G., Loncarich, and J.T. Swaim, 1992, "CASTFOREM (Combined Arms and Support Task Force Evaluation Model). Update: Methodologies", Department of the Army Technical Documentation, TRAC-WSMR-TD-92-011.

[3] Wetmore, A. and S.D. Ayres, "COMBIC-Combined Obscuration Model for Battlefield Induced Contaminants", US Army Research Laboratory Technical Report, ARL-TR-1831, August 2000.

[4] Sutherland R.A., 2002, "Determination and use of IR band Emissivities in a Multiple Scattering and Thermally Emitting Aerosol Medium", U.S. Army Research Laboratory Technical Report, ARL-TR-2688, July 2002.

radiometer measurements were in good qualitative agreement with PILOT81 over all optical depths considered; however, the quantitative performance was improved by “tweaking” the results using semi-empirical emissivity and reflectivity functions in place of the more theoretically rigorous multiple scattering solutions developed (strictly) for isothermal clouds of radial symmetry. The experiments were limited in scope to two emissive smoke types and obscurant temperatures of a few degrees above ambient.

1. Introduction

Possibly the two most important radiative parameters needed to characterize the effects of airborne obscurants on the performance of modern IR systems is the direct beam transmittance and the integrated path radiance. Together, these two parameters can be used to model the total radiant signal available at the entrance aperture of the receiver a given optical system as:

$$I_{rec}(\tau) = I_{tgt} T_i(\tau) + I_{bkg} S(\omega_i, \tau) \tag{1}$$

where τ is the obscurant optical thickness, $T_i(\tau)$ is the direct transmittance, ω_i is the obscurant single scattering albedo and the index 'i' refers to the particular receiver spectral bandpass of interest (tab. 2). Defined as such, the first term in eq 1 represents that fraction of the received signal having originated from some "hard" target of surface radiance, I_{tgt}, that reaches the receiver essentially unimpeded by the intervening medium (i.e., direct transmission) and the second represents all other "stray" contributions from the aerosol cloud and/or the ambient surroundings at all points along the propagation path (i.e., path radiance). In eq 1, the (normalized) path radiance function, $S(\omega_i;\tau)$, is generally comprised of two parts accounting for both the reflective and emissive properties of the aerosol cloud as:

$$\begin{aligned} &\text{path radiance function :} \\ &S(\omega_i;\tau) = a_i R(\omega_i;\tau) + b_i E(\omega_i;\tau) \end{aligned} \tag{2}$$

where the first term accounts for all contributions due to in-scatter originating from the ambient surroundings, and the second accounts for all contributions originating from thermal emissions internal to the aerosol cloud. In writing the above expressions as such, ambient inputs were assumed to be isotropic and the obscurant temperature can be treated as uniform. These approximations are made for convenience in establishing manageable guidelines for the analysis of the field data to follow and do not necessarily reflect any limitations on the scope of the study. A more complete description of the underlying theory and the physical processes involved is given in the PILOT81 documentation (*1*). With this being the case, the parameters, a_i and b_i become the sole ambient drivers representing, respectively, the atmospheric sources for in-scatter and the aerosol (obscurant) sources for thermal emission. For IR scenarios it is furthermore customary to express these parameters in terms of their equivalent blackbody temperatures as:

$$\begin{aligned} &\text{atmospheric drivers :} \\ &a_i = \frac{F_i^*(T_{amb})}{I_{bkg}} \frac{\sigma T_{amb}^4}{\pi};\quad b_i = \frac{F_i^*(T_{cld})}{I_{bkg.}} . \frac{\sigma T_{cld}^4}{\pi} 3) \end{aligned} \tag{3}$$

where T_{ext} and T_{cld} represent the equivalent blackbody temperature (absolute) of the ambient atmosphere and the aerosol cloud, respectively, and the functions $F_i^*(T)$ represents the calculated fractional blackbody irradiance within the particular spectral band of concern. It may be noticed in eq 3 that the "background" radiance, I_{bkg}, as used here turns out to be a simple

normalizing factor that actually "cancels out" when used in eq 1. Later this parameter will be associated with "clear air" radiometer measurements in the analysis.

In all of the above expressions and those to follow, the obscurant optical thickness, or optical depth, τ , is the independent variable representing the obscurant and is defined formally in terms of the path integrated aerosol concentration and is related to the Beer's Law for direct transmittance as:

$$\begin{aligned} &\text{transmittance}: \\ &T(\tau) = \exp(-\tau) \\ &\text{optical thickness;} \\ &\tau = \alpha_i \int_o^L C(r')dr' \end{aligned} \tag{4}$$

where C(r´) represents the aerosol mass concentration at any point, r´, along the target-receiver path of propagation, and L is the total path length. The (band dependent) obscurant mass extinction coefficient, α_i, accounts for both absorption and out-scattering along the path [i.e., $\alpha=\alpha_{abs} + \alpha_{sct}$] and is related to the single scattering albedo as [$\omega=\alpha_{sct}/(\alpha_{abs}+\alpha_{sct})$]. In applications, the path integral in eq 4 is sometimes referred to as the "concentration path length", or simply the "CL Product" and is a property of the aerosol mass properties, independent of the receiver bandpass. Reasonable estimates of the optical properties of a wide range of military obscurants can be found in the COMBIC documentation (*2*).

The main purpose of the analysis described herein was to develop and test methods for determining the relationships between the obscurant optical thickness, the direct transmittance, and the normalized path radiance using measurements obtained from the SLAD or MPTR, system (*3*). As it happens, methods for determining the obscurant direct transmittance have been developed and refined over the years in the course of the various Smoke Weeks conducted by the U.S. Army and summarized in detail elsewhere (*4*). However, methods for determining the path radiance are not as well understood and there is little quantitative data available, especially for wavelengths in the IR where the effects of both multiple scattering and thermal emission can be important. Despite this dearth of information, it is nevertheless important to realize that for emissive sources it is actually the (interfering) path radiance that can limit system performance and not necessarily the directly transmitted signal alone, a fact that has often been overlooked in the past but one that has again been addressed in recent experimental studies (*5*). It is this latter deficiency that is most fully addressed in this report.

The ultimate application for the analysis here is to improve the representation of emissive obscurant effects in scene simulations models such as SCIMITAR (*6*), systems performance models such as TARGAC (*7*), and wargame simulations such as CASTFOREM (*8*).

In the remainder of the report, sections 2, 3, and 4 are used to describe the experimental set-up, develop the MPTR theory, and present examples of actual field measurements. Section 5 includes a brief description of the use of the aerosol emissivity and reflectivity functions, both theoretical and semi-empirical, and the rationale behind the Log R/T correlation methods for extracting the aerosol transmittance and path radiance from the MPTR data. Sections 7 and 8

present an overview of the entirety of the multi-trial experiments using both the MPTR and the supporting IR imagery. In the final section we demonstrate utility of the results in modeling emissive obscurant effects using semi-empirical methods, explain the relationship of the MPTR measurements to the sky-to-ground parameters used in the older models, and discuss the limitations of the of other modeling approaches based on linear approximations. There are four appendices; the first three providing details of the MPTR measurements and the fourth giving more detail on the use of conventional IR imagery.

2. Overview of the Experiment

A unique and defining feature of the experiment was the simultaneous measurement of direct transmission and total radiance over multiple paths and multiple spectral bands through artificially generated aerosol clouds of varied optical thicknesses. Radiative measurements were performed with both the MPTR system and a research grade dual band IR imager. The experiments were conducted near the SLAD 100 ft tower site at the White Sands Missile Range, NM. The general experimental layout is shown in figure 1.

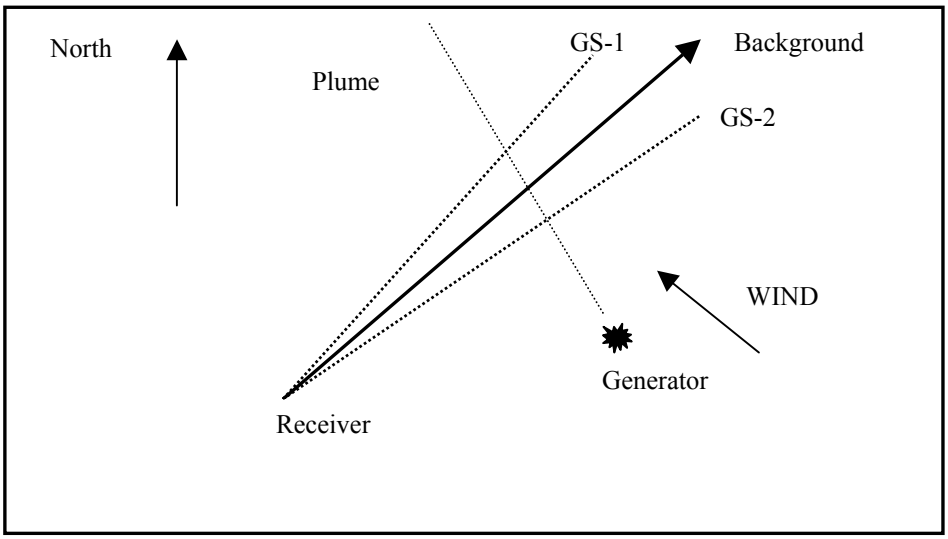

Figure 1. Sketch of field set-up at the SLAD 100 ft tower site.

Key elements of the experiment were; (a) three horizontal sampling lines, two for transmission, one for radiance, (b) a variable rate aerosol generator for either brass or graphite, (c) supporting meteorological measurements, (d) visible band video documentation, and (e) supporting IR dual band imagery.

2.1 General Layout

In the figure. 1, the central line of sight (bold arrow) was directed outward along a heading of roughly 44°and was the main path over which the MPTR total radiance was measured against the distant natural background. Simultaneous measurements of direct transmission were performed along the two outer (dashed) paths terminating at the locations labeled GS-1 and GS-2 where the MPTR guide sources were located. The total distance from the MPTR receiver to the guide sources was about 525 m and the angle separating the two transmissometer paths was approximately 4°. In all cases the lines of sight were parallel to the (earth) surface and fixed at a height of 2 m. All transmission and radiance measurements were synchronized to within about 1/10 s and were carried out simultaneously over the four spectral bands identified in table 1.

Table 1. Identification of MPTR Bandpasses.

Band 1: $\Delta\lambda_1$=0.40-0.70 um, visible
Band 2: $\Delta\lambda_2$=1.06 um, near infrared
Band 3: $\Delta\lambda_3$=3-5 um, mid infrared
Band 4: $\Delta\lambda_4$=8-12 um, far infrared

The experiments (eight trials total) were carried out in a single day over the course of about 90 min under generally fair weather conditions (see meteorological data later). The aerosol generator was located at a point about half the distance between the MPTR receiver and the transmissometer guide sources and from 25 to 50 m upwind of and generally perpendicular to the main path- the exact distance and location depending upon the wind speed and direction.

2.2 Description of Trials

There were eight full trials of roughly 6 min duration each and all conducted successively in alternating pairs of either graphite or brass powder using the general scheme of table 2.

Table 2. Trial data for 16 February 1999.

Trial No	Start	End	Type	R(#/m)
21601	12:45:59	12:55:56	Dust	N/A
21602	12:56:59	13:08:28	Graphite	10.0
21603	13:09:45	13:23:12	Brass	10.0
21604	13:24:14	13:34:17	Graphite	8.0
21605	13:34:59	13:45:27	Brass	8.0
21606	13:46:29	13:58:22	Graphite	4.0
21607	13:59:15	14:09:27	Brass	4.0
21608	14:09:59	14:20:27	Graphite	2.0
21609	14:20:59	14:31:28	Brass	2.0

The first column in table 2 identifies the trial number by date (216) and set (01through 09), the next two columns identify the precise time of day (Mountain Standard Time (MST)) for the start and end of each trial, the fourth column identifies the obscurant type, and the fifth column gives the generator mass emission rate setting. As noted, the generator mass emission rate for the first pair of trials was set at 10 lb per minute (the maximum used) and then adjusted incrementally downward to a minimum of 2 lb per minute for the final set. The first trial was a "shakedown" run using locally generated dust and is not included in the formal analysis. The main trials were conducted in rapid succession in an attempt to complete all of the experiments during nearly constant meteorological conditions (see meteorological data later). The general appearance of the obscurant clouds is demonstrated in the photographs of figure 2 which were taken with a commercial visible band digital camera.

Figure 2. Photographs of test site and smoke generation.

The two upper photographs in figure 2 were taken from near the top of the 100 ft tower looking generally eastward and downward along the main sampling path and the lower two were taken from ground level near the base of the tower. In both cases the left photograph refers to brass and the right refers to graphite. In the uppermost photographs, the aerosol generator and supply vehicle can be seen to the immediate right of the aerosol plume. Other objects are the bare dirt

road, power poles, and a variety of other natural and manmade features in the background. In the lower photographs, the large object in the foreground is the blackbody source used for calibration and the two bright lights most apparent at the left and right extremities in the brass example are the MPTR guide sources at the locations labeled GS-1 and GS-2 in figure 1.

The brass powder produced a visibly bright, brownish, cloud similar in color to the appearance in bulk samples. Likewise, the graphite powder produced a visibly dark, nearly black, cloud with occasional patches of a light gray most often seen near the cloud edges. In all cases the method of aerosol generation produced reasonably well-defined, semi-continuous plumes of about the size and concentration expected and with the characteristic internal chaotic structure characteristic of such clouds when generated in the real (turbulent) atmosphere. Overall the plumes were well behaved in that they were constrained to near the ground and maintained a reasonably coherent large scale structure over the testing distance. However, some cases of local vertical lofting could be seen in the visible band imagery which most often occurred for the graphite trials at points nearest the generator and was later evidenced in the transmissometer data.

2.3 Meteorological Measurements

The weather during the earlier part of the week of the experiments was characterized by strong frontal activity that caused excessively high winds the day prior to the experiments; however, by the time the trials were conducted the conditions had changed to generally fair and cloud free with light to moderate winds. Figure 3 shows the on-site measurements for the full diurnal period that were obtained from a mobile van located approximately 100 m southwest of the main area.

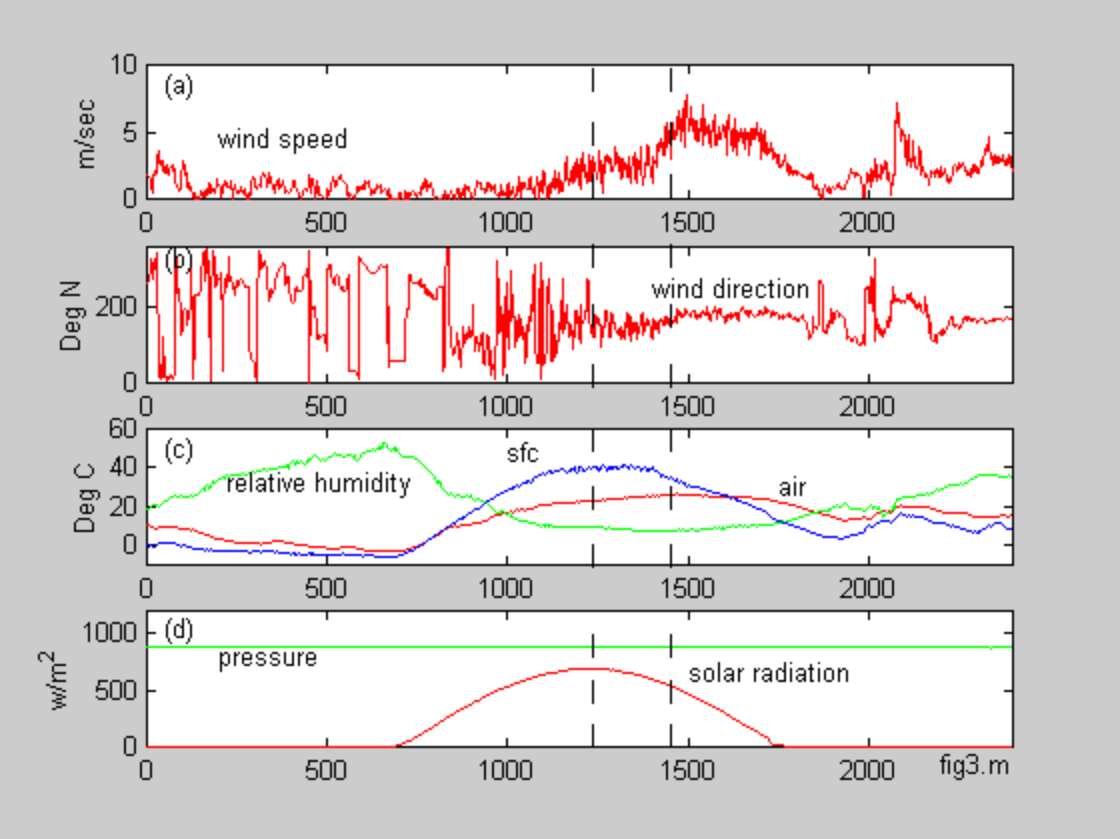

Figure 3. On site meteorological measurements.

With reference to the measurements shown in figure 3, the winds during the morning were light and variable in both speed and direction making it more or less unsuitable for testing because of the problems encountered in correctly placing the aerosol generator such as to intersect the instrumented line. By the afternoon, however, the winds had stabilized noticeably and eventually settled in to a direction consistently from the south (180º) in general agreement with the forecast from the nearby range "C" station. The time period during which the experiments were conducted are indicated by the vertical hash marks in figure 3. As noted, the experiments were started near 1130 hrs (MST) shortly after the winds had stabilized to a mean speed of about 3 m/s; however, they did increase during the course of the experiment to a value of about 5 m/s by the end. This timeframe was slightly past local noon, thus the sun was near apex at about 30º south roughly along the same heading as the plume centerline and perpendicular to the main sampling line. According to the radiometer data, the solar (direct + diffuse) irradiance that day was at a midday maximum of about 650 W/m^2 during the beginning of the experiment and decreased to about 600 W/m^2 by the time the trials were completed. Air temperature was nominally about 45 C at the beginning and dropped to about 40 C by the end.

3. MPTR Field Data Reduction

The SLAD MPTR system as employed for this test provides a measure of the total radiance against a natural background over a central line of sight plus a measure of the direct radiance from the guide sources over two adjoining lines of sight as noted previously in figure 1. Prior to the analysis, the raw signals are subjected to a certain amount of calibration, normalization, and manipulation to compensate for clear air atmospheric effects so that the reduced data is representative solely of the aerosol cloud. In the final analysis, the data are used to yield estimates of the relative transmittance and normalized path radiance as defined in the introduction of section 1. The methods for doing this are described in detail in appendix A. In this section the process is discussed in somewhat abbreviated detail using the examples of raw data plotted in figure 4 as a reference.

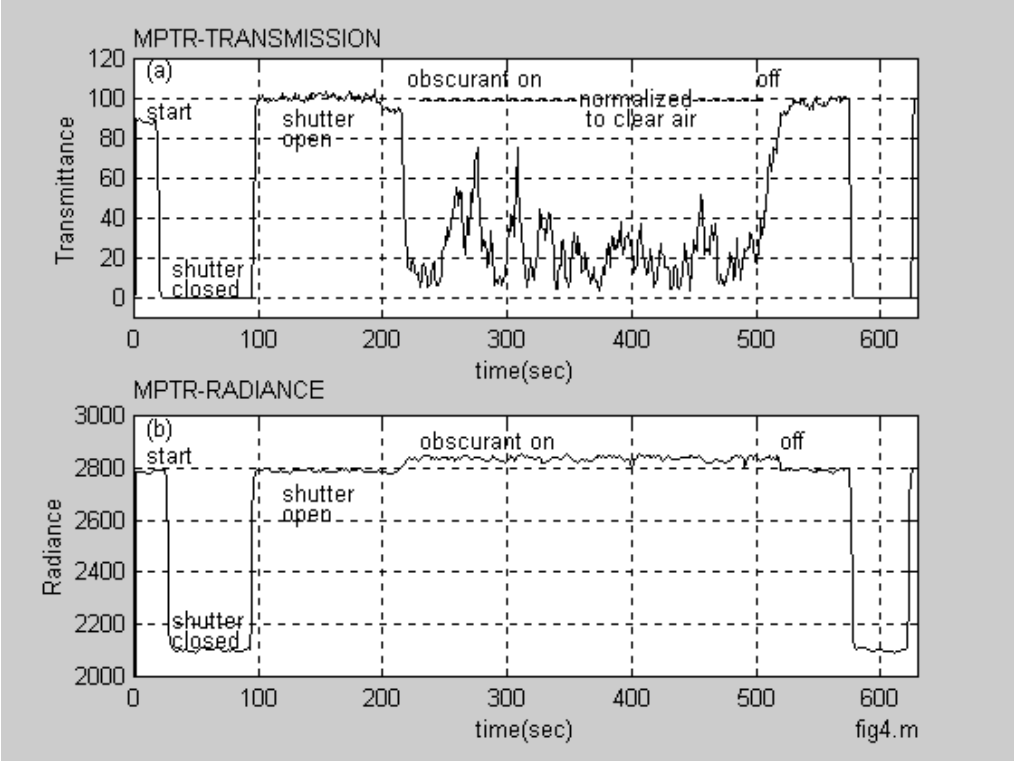

Figure 4. Examples of MPTR signals for (a) transmissometer mode and (b) radiometer mode.

In figure 4, the upper sketch refers to the transmissometer mode (trial 21608, graphite) and the lower sketch refers to the radiometer mode (trial 21609, brass). As indicated, a typical trial takes about 5–7 min (i.e., 600+ s), which includes time for both data collection during the (smoke) event and time before and after to allow for calibration. The onset and duration of these various time periods, annotated on the figure, are usually clear from inspection of the raw signals and are evidenced by a sudden changes in signal level; these time periods will not be overly elaborated on in this section. Both sets of data were taken in the visible band and are discussed more fully in the following paragraphs.

3.1 Transmissometer Mode (Figure 4a)

In normal MPTR operation all raw transmissometer signals are calibrated and scaled in the field to give real time measures of what is called the relative (aerosol) transmittance. The calibration process involves taking measurements for some short time period before (and sometimes after) each trial. These data are then used to "normalize" the signal to the clear air readings. More details are given in appendix A but the procedure ultimately produces a time dependent relative transmittance, $T_i(t)$, extracted from the raw data as follows:

$$T_i(t) = \frac{X_i(t) - X_{min}}{X_{max} - X_{min}} \tag{5}$$

where $X_i(t)$ represents the raw (voltage) signal received in one of the four optical channels identified previously in table 2 (i.e., i=1,4) and t is elapsed time.

The scaling parameters, X_{max} and X_{min} , are obtained from readings taken in the time period just prior to the release of the obscurant. In the example of figure 4a, the first 20 s or so labeled "start" represent the initial clear air reading to determine X_{max}, which is followed immediately by a nominal 60–80 s time period labeled "shutter closed" to determine a "zero" reading, X_{min}. The net effect of eq 5 is thus to produce a signal "normalized" to the clear air value such that the new clear air reference is set to 100 percent. Note that this normalization procedure also eliminates the need to know the actual value of the radiance from the guide sources. After another short period of clear air readings labeled "shutter open," the obscurant is released and reaches the sampling line a short time later as evidenced by an immediate decrease in the signal at the point labeled "obscurant on."* (After some specified elapsed time (five min for these trials), the generator is turned off, and the signal slowly rises as the smoke clears as is evident near the end of the trace in the region marked "off". Although the effects of generator fluctuations cannot be entirely ruled out, the intense and very rapid fluctuations in the signal during the time that the obscurant is on is due, for the most part, to mechanical wind turbulence as it affects aerosol concentration and is often observed in experiments of this type when conducted during daytime conditions.

Calibrated and scaled as such the reduced signal now represents the aerosol transmittance from which can be immediately calculated the optical depth and path integrated concentration as a function of time using the inverted form of Beer's Law, that is:

$$\begin{aligned} &\text{optical thickness :} \\ &\tau_i(t) = -\text{Ln}[T_i(t)] \\ &\text{path concentration :} \\ &CL(t) = \frac{1}{\alpha_i}\tau_i(t) \end{aligned} \tag{6}$$

*The initial and less pronounced signal reduction just prior to the obscurant release is an artifact due to dust and other debris created by the generator startup and is to be ignored in the analysis.

where it is to be noted that the CL product, being a measure of the obscurant mass, is independent of the particular bandpass selected and thus should yield the same result for all four optical channels. Note also that the CL product cannot be determined from the transmittance measurements alone unless there is an independent measurement of α_i, the band-dependent mass extinction coefficient (assumed to be a constant for a given spectral region and independent of time). In calculating the CL product for later use, an average was computed based on all four spectral bands assuming a known value for the mean as determined from laboratory data. This data, for the record, were taken to be $<\alpha>= 1.0$ (m^2/gm) for brass and $<\alpha>=1.45$ (m^2/gm) for graphite. These and other assumptions concerning the obscurant optical behavior are discussed in later sections.

3.2 Radiometer Mode (Figure 4b)

The initial steps in the radiometer mode are very similar to those of the transmissometer mode. However, in this case there are no artificial guide sources in the path so that the pre-event readings in this case correspond the clear air readings taken against the natural background. Thus the corresponding equation for the radiometer mode is identical in form to that of eq 5, that is:

$$R_i(t) = \frac{Y_i(t) - Y_{min}}{Y_{max} - Y_{min}} \tag{7}$$

where, in this case $Y_i(t)$ represents the time-dependent radiometer signal. The scaling parameters Y_{min} and Y_{max} are obtained in the same manner as before using the pre-event opened and closed shutter readings. In figure4b, it is interesting to note that in this case the signal actually increases when the obscurant (brass) is introduced. This indicates that the loss in signal due to extinction (i.e., lower transmittance) is more that compensated by the gain in signal due to the path radiance. However, in most other cases, the IR in particular, the obscured signal is more likely to decrease as will be seen in later examples.

With the raw data so calibrated the resultant signal now represents a measurement of the total received radiance (actually normalized to the clear air) discussed in section 1. The next task is to separate out the transmittance and path radiance contributions using the basic relationship of eq 1. There is a problem because measurements are not all collinear; however, any errors are minimized provided that the obscurant concentration distributions over the three sampling lines are not inordinately different. Thus, it is valid to calculate the path radiance from the measured data by performing a point by point differencing at each time interval using the simultaneous measurements from all three paths, ignoring for the moment the slight delay due to obscurant transport. That is, using and rearranging the time-dependent normalized version of eq 1, for each time sample, t, the result is:

$$\begin{aligned} &\text{path radiance :} \\ &S_i(t) = R_i(t) - T_i(t) \end{aligned} \tag{8}$$

where the total radiance, $R_i(t)$, is obtained from the radiometer sampling path and the transmittance, $T_i(t)$ is obtained by averaging over the two transmissometer paths. At this point it is also necessary to assume that the time lag for obscurant transport between the sampling lines is small compared to the averaging time which is the same as assuming that the measurements are essentially time synchronized. The fact that these conditions are approximately maintained

was qualitatively verified from the imagery data and more quantitatively from the correlation analysis discussed in later sections.

4. Examples of Field-Processed Data

Before proceeding to the actual analysis it is worthwhile to examine some general trends that become more or less immediately apparent from casual inspection of the field-processed raw data. The example for graphite (trial 21608) shown in figure 5 will serve as a reference for discussion.

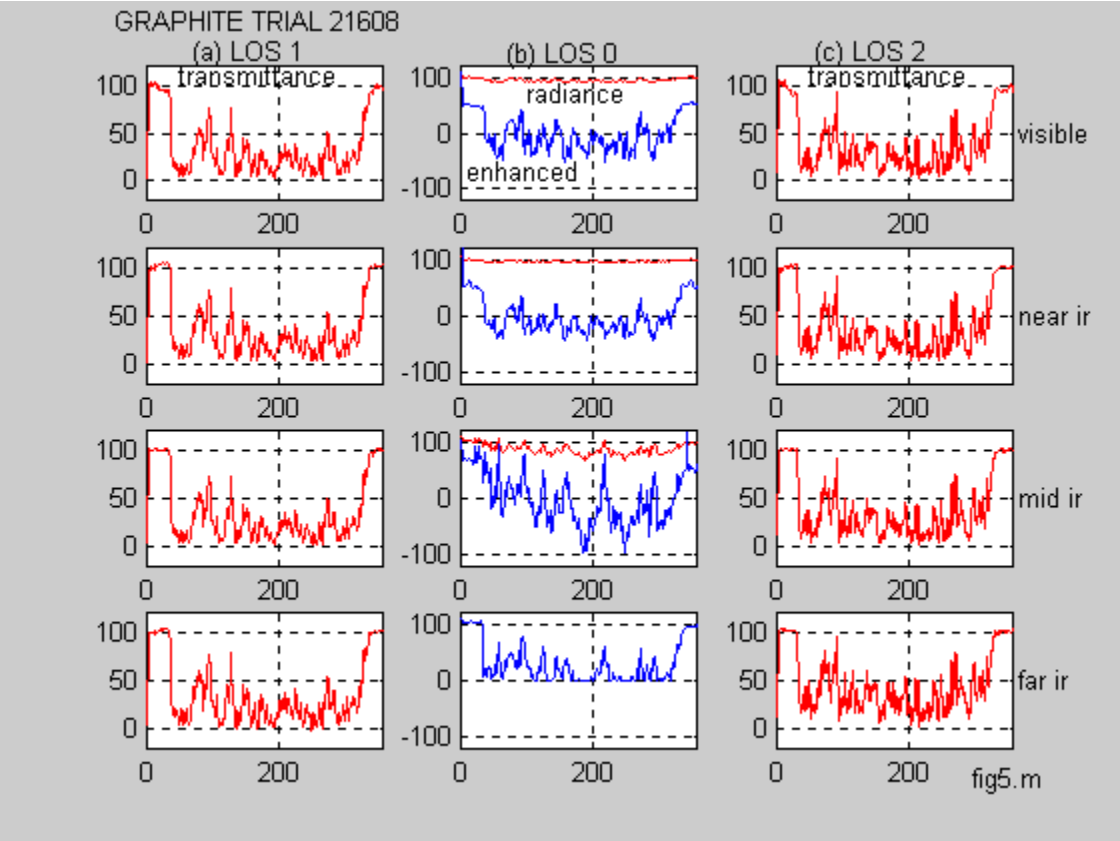

NOTES:

(a) LOS-1relative transmittance measurements performed over LOS-1
(b) LOS-0 total radiance measurements performed over LOS-0
(c) LOS-2 relative transmittance measurements performed over LOS-2

Figure 5. Example of multi-band MPTR field data (trial 21608, graphite).

In all cases (fig. 5), the introduction of the obscurant marking the beginning of the event near the 60 s mark and the ending some 300 s later is immediately evident from the traces and need not be elaborated upon further. The four rows in each matrix correspond to the four spectral bands identified table 1. Note that the center column, (b) LOS-0, shows both the original, nearly featureless, total signal plus a mathematically "enhanced" version that shows more detail in the fluctuations.

4.1 Transmittance Data

Perhaps the most distinctive feature seen in the measured data is the fact that the transmittance traces for all four bands are nearly identical for each of the two transmissometer lines of sight. This statement applies not only to the overall magnitude of the signal but also to the details of the fluctuations. This observation was later found to be true for all trials, both brass and graphite, and is not necessarily unexpected since it is known from other sources that the mass extinction coefficients for both obscurant types are nearly independent of wavelength (*2*). It is somewhat more interesting to note that there is also a high degree of correlation between the traces for the two (separated) transmissometer paths. This, too, is not entirely unexpected since, in both cases, the measurements are based on the same cloud sampled over slightly different paths, but it does attest indirectly to the consistency of the data in the sense that there appear to be no artifacts brought about by faulty sampling techniques. It is also noteworthy that the transmittance along the path nearest the generator source (i.e., upwind, LOS-2 is slightly higher than that along the farther downwind path (i.e., LOS-1). This difference was more evident for graphite than for brass and was probably due to aerodynamic and thermal lofting of the cloud as a whole which was also observed in the video data. Another observation of some interest is the fact that the path nearest the source has some very high frequency components that appear to be damped farther downwind which may be indicative of the increased mixing generally predicted by diffusion theory. Overall the same general behavior describe here was also observed for brass (not shown) although it was consistently found that, for a given trial pair, the mean transmittance for graphite was lower than that for brass which is consistent with other findings on the relative magnitude of the mass extinction coefficient for the two obscurant types discussed earlier.

4.2 Radiance Data

Looking first at the two shorter wavelength bands, perhaps the most immediate and distinctive feature of the (unenhanced) radiance plots of figure 5 is the fact that the measured total radiance is almost unaffected by the introduction of the obscurant. This behavior was noted previously and is an indication of the near zero balance between the competing processes of signal attenuation and path emission which actually resulted in a net increase in total radiance for the case of brass that was noted earlier (fig. 4b). For the graphite sample, however, the signal is reduced in both cases indicating that attenuation is the more dominant mechanism although the difference is small. The enhanced plots show that the net effect is about the same for the visible and the near IR bands, even in the details of the fluctuations.

At the longer wavelengths it appears that attenuation becomes relatively more significant as evidenced by the fact that both traces decrease when the obscurant is introduced, much more so for the far IR band than for the mid-IR band. However, at this point it becomes clear that the far

IR signal has approached the lower threshold of the MPTR sensitivity as evidenced by the consistent "capping out" at low signal levels. This effect was even more evident from the other trails and for this reason the far IR data from the MPTR was not used in the analysis. However, the qualitative aspects of the data were later verified with the thermal imagery where it was observed that total radiance in the far IR band was consistently lower that in the mid IR band as discussed in more detail in section 8.

Another interesting feature seen from the radiance plots is the near perfect correlation in the fluctuations between the visible and near IR bands which is most clearly shown in the enhanced plots. The same may be said of the correlations between the mid- and far IR bands although the evidence is less convincing due to the problem with the threshold. It is reasonably clear, however, that the correlations between the longer and shorter bands are not nearly as strong. For brass (not shown), the cross-band correlations in total radiance were not nearly as strong as for the graphite example for any of the bands studied. The reasons for the specific behavior are not totally clear but may be due to the fact that the dominant mechanisms at the shorter wavelengths

derive mainly from ambient in-scatter while those at the longer wavelengths derive mainly from internal thermal emission. In a later section the correlations are analyzed analytically using all trials.

---

5. Analytical Methods

In this section the theoretical framework is reviewed and analytical procedures brought to bear in the analysis of the experimental data. The underlying assumptions are; (*1*) that the processed field measurements do indeed provide an accurate measure of multi-band transmittance and the corresponding (near) simultaneous multi-band path radiance for each of the spectral bands considered, (2) that the transmittance data can be tested in terms of the Beer's Law relationship, and (*3*) that the path radiance results can be explained using semi-empirical methods based on theoretical calculations of emissivity and reflectivity. There is, of course, the possibility that the data may contain new findings beyond the scope of existing theory. It is thus left for the analysis to provide the means necessary to test the various relationships predicted by existing theory and to determine tests for validating new findings.

For the direct transmittance measurements, the applicable method is the well known "Log-T" correlation technique which essentially tests the data against the Beer's Law relationship. For the path radiance measurements, the methods are not so well-known and necessitated the invention of an analogous new technique, which we called the Log-R method that essentially exposes departures from "ideal" linear behavior. Semi-empirical methods were then developed based on exact calculations supplied by PILOT81 model which was compared with the measurements.

5.1 Multiple Scattering Emissivity and Reflectivity Functions

The difficulty in applying the expressions of section 1 to the task at hand lies in the fact that the emissivity and reflectivity functions are generally not known from measurements and are difficult to calculate in real world applications. However, it is possible to generate exact

solutions that are rigorous for certain idealized situations that might be similar to those of the real world that can be used as guidelines for the analysis and this is the philosophy behind the semi-analytical approach taken here.

For a homogeneous and isotropic cloud of radial symmetry, the emissivity and reflectivity functions can be computed exactly over any path through the cloud from integral expressions of the following form (*1*):

$$\text{emissivity}: \quad E(\omega,\tau) = \int_{o}^{\tau} J'(\omega;\tau')e^{-\tau'}d\tau' \tag{9}$$

where $J'(\omega;\tau)$ is the so-named emissive source function, generally obtained from models such as PILOT81 (*1*), and τ is the optical thickness as calculated over the total length of the target-receiver path. A similar calculation can be performed for the reflectivity function; however, for an isothermal cloud, it is simpler to use the following conservation relationship:

$$\text{isothermal clouds}: \quad E(\omega;\tau) + R(\omega;\tau) = 1 - T(\tau) \tag{10}$$

where the expression on the right side is identical to the classical definition of absorptivity, (i.e., $A(\tau)=1-T(\tau)$), although this terminology is something of a misnomer since the transmittance accounts for both absorption and out-scattering. Equation 10 is valid for all spectral bands and all cloud geometries but, as noted, is strictly applicable only for the case of isothermal clouds and the condition of isotropic scattering.

Some plots of the emissivity and reflectivity functions for optical depths up to $\tau=4$ based upon source functions obtained with PILOT81 are shown in figure 6.

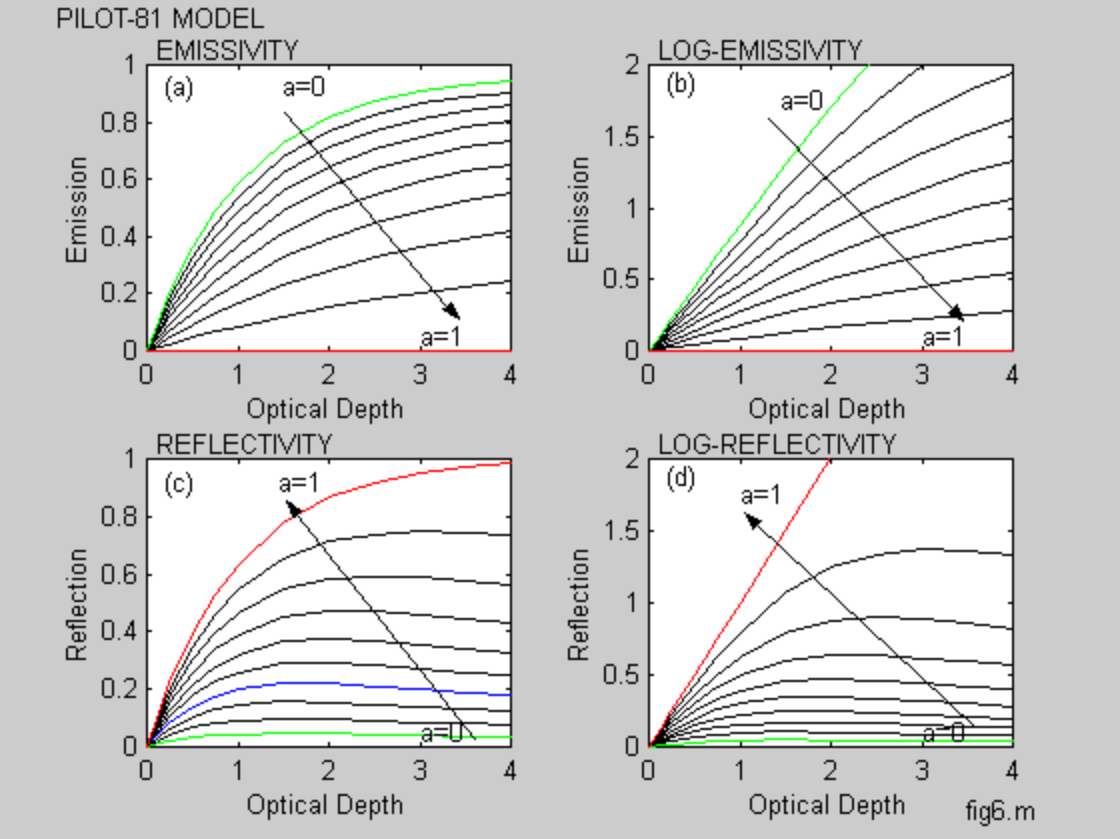

Figure 6. Theoretical calculations of emissivity and reflectivity (*1*).

As is evident from inspection, the functions are well-behaved and predictable in the sense that all curves increase monotonically with increasing optical depth, being somewhat linear in the beginning and then leveling off as the optical depth increases to the point becoming more or less insensitive to changes at the higher values. Note the similarities but also the reversal of the ordering of the curves for albedo in the two cases. The logarithmic plots are shown here for later reference and are useful in that they demonstrate a linear tendency, especially for the emissivity case and smaller values of optical depth and the extremes of albedo.

5.2 Beer's Law and Linear Models

Perhaps the simplest approximation that can be applied for the analysis is to assume the source function , J′(ω;τ), to be constant over the path of interest. In this case the integration in eq 9 can be performed immediately to yield the following simple Beer's Law form for the normalized path radiance.

Beer's Law (path radiance):

$$S_i^0(\tau) = [1 - T_i(\tau)] \qquad (11)$$
$$= [1 - exp(-\alpha_i CL)]$$

where the superscript ‘o’ is used to denote “zeroth’ order and the transmissivity is expanded in terms of the obscurant mass extinction coefficient and CL Product. The Beer’s Law is referred to as a “linear” model, in part, because it is linear with respect to transmittance, but, of more importance, is the fact that it is also linear with respect to the logarithm [Ln(1-S)] , the significance of which will be made more clear later in this section. Despite the simplistic appearance and limited range of validity, the above expression plays a central role in modeling and analysis.

5.3 Semi-empirical Methods

For thin optical depths and for some other special cases, the Beer’s Law, or “linear” form given by eq 11 is sufficient for estimating path radiance; however, for the more general case involving both thermal emission and multiple in-scatter the need for a more comprehensive approach is anticipated and, thus, define a higher order semi-empirical “intuitive” approximation based on the general form of the plots of figure 6 as follows:

$$\begin{aligned} &\text{semi - empirical :} \\ &E(\tau) = \beta[1 - exp(-\frac{\tau}{\tau_2})].....\text{emissivity} \\ &R(\tau) = A(\tau) - E(\tau).....\text{reflectivity} \\ &A(\tau) = 1 - exp(-\frac{\tau}{\tau_1}).....\text{absorptivity} \end{aligned} \tag{12}$$

where the various constants [β,τ_1,τ_2] are empirically based, band dependent, scaling parameters to be derived from the analysis. In practice, it was found that these functions did an accurate job in maintaining the overall qualitative features of the rigorous solutions while at the same time offering a more flexible basis for analysis.

5.4 Transmissometer Analysis, Log-T Method

The Log-T correlation technique is an often-used method for analyzing transmittance measurements and is based solely on the Beer’s Law of extinction. Briefly, the approach is to first define a test metric, $Z_i(t)$ as follows:

$$\begin{aligned} &\text{Ln T Correlation Method :} \\ &Z_i(t) = -Ln[T_i(t)] \end{aligned} \tag{13}$$

where $T_i(t)$ represents the (time dependent) measured transmittance as determined in the manner described in section 3 . It is clear from inspection that a point by point plot of $Z_i(t)$ versus CL(t) should, if all assumptions are correct, yield a straight line intersecting the origin with a slope equal to the value, α_i , the obscurant mass extinction coefficient for the spectral band of interest. This is the essence of the Log-T correlation method and an example of how it works using real measured data is demonstrated in figure 7.

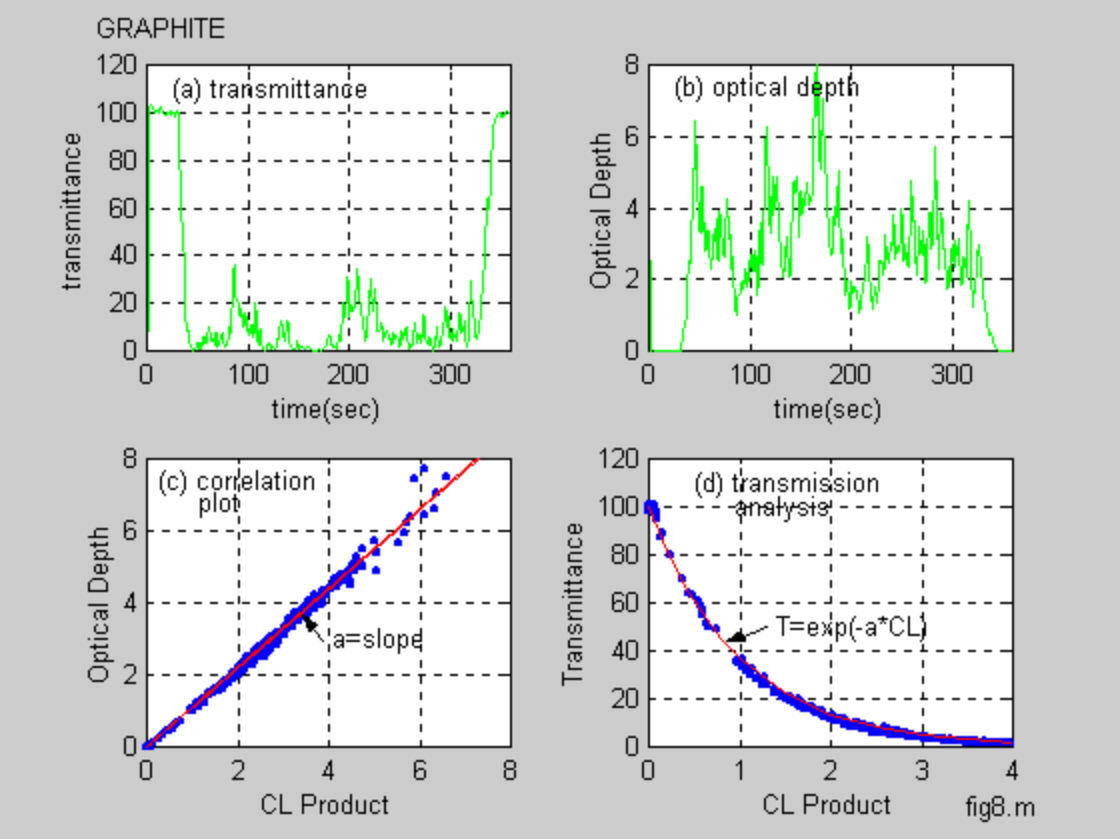

Figure 7. Demonstration of the Log T correlation method applied to the MPTR transmissometer data.

In figure 7, the upper plot labeled (a) is taken as the starting point and shows the raw time dependent transmittance measurements taken, for this particular example from Trail 21604 (graphite). The next step, illustrated in the plot labeled (b), is to compute the test variable, $Z_i(t)$, using the logarithmic expression of eq 13 at each time step. Next the test variable, $Z_i(t)$ is plotted versus CL(t) in the plot labeled (c), which is the essence of the Log-T correlation method for which the result here does indeed indicate a clear linear relationship as expected. In this case, the analysis yields a slope slightly greater than unity, indicating that the mass extinction coefficient for this particular spectral band is somewhat smaller than the mean. The last plot labeled (d) is formed by inverting eq 13 to recover the point-by-point transmittance plus the corresponding Beer's Law analytical fit. The particular results here are more or less representative of all trials which, when taken together, give convincing evidence of the validity of the theory and the various underlying assumptions, more of which will be discussed in later sections.

5.5 Radiometer Analysis, Log-R Method

The Log-R correlation approach is similar to the Log-T approach except that the underlying framework is based on the Beer's Law expression for attenuation [i.e., A(τ)=1-T(τ)] rather than extinction. The analogous test metric in this case becomes:

$$\text{Ln R Correlation Method :}$$
$$Z_i(t) = -Ln[1 - S_i(t)] \tag{14}$$

where $S_i(t)$ is the normalized path radiance. The rationale behind this particular choice of test metric lies in the form of the zeroth order solution of eq 11. That is, upon taking the appropriate logarithm as suggested by eq 14 and following through with the Beer's Law expression, a point-by-point plot of the new metric, $Z_i(t)$, versus CL(t) should, if the assumptions are correct, yield a straight line intercepting the origin and, as before, with slope equal to the value of the mass extinction coefficient. Of course deviations from a straight line then indicate departures from the underlying assumptions, the most likely involving issues of thermal emission, multiple scattering, and combinations thereof not treated in the linear approximation. An example of how the method works using real measured data from trial 21606 (graphite) is shown in figure 8.

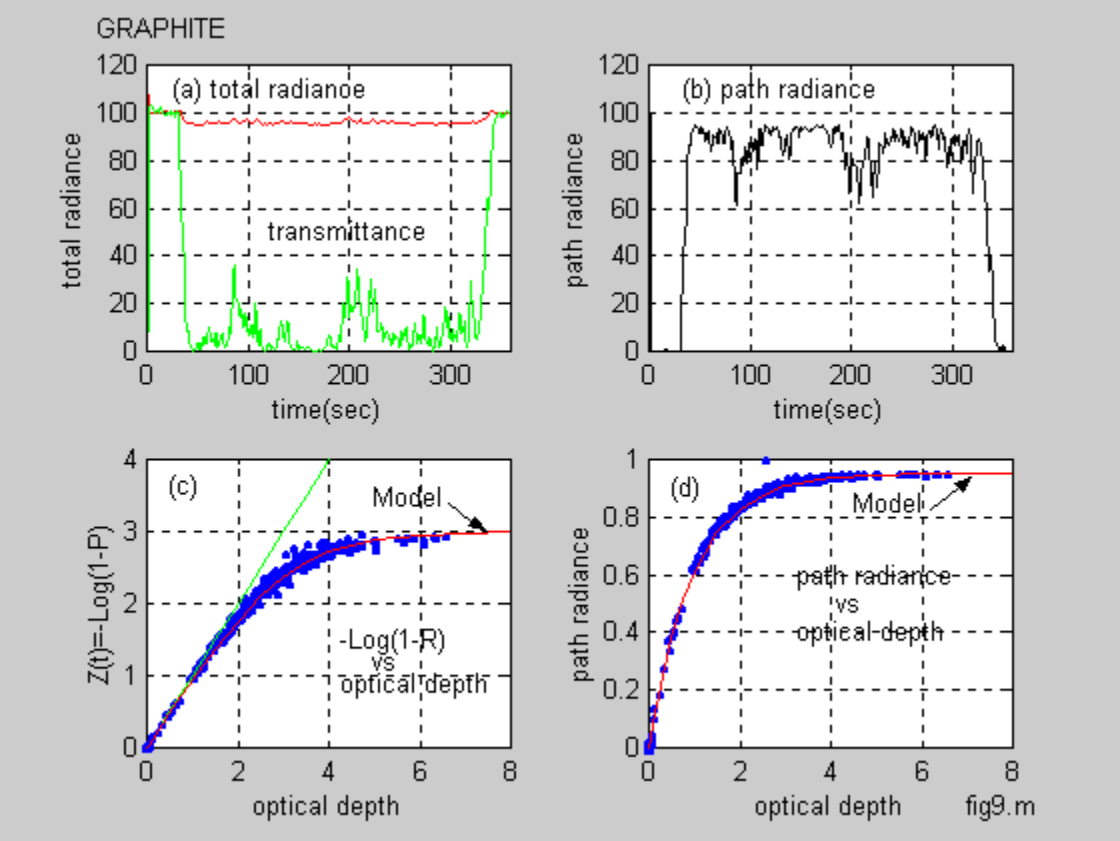

Figure 8. Demonstration of Log-R correlation method applied to MPTR radiometer data.

In this case, the starting point, labeled (a) in figure 8, is represented by a plot of the total radiance plus the corresponding transmittance (taken as the average over the two transmissometer paths). The next step is to subtract the direct transmittance from the total radiance to obtain the normalized path radiance in accordance with the discussion leading up to eq 8 in section 4. The result from this step is shown in the plot labeled (b) where the interesting fact is noted the that the path radiance in this cases accounts for approximately 70–80 percent of the total radiance. The next step is to take the appropriate logarithm and form the correlation with optical depth which is shown in the plot labeled (c), and in inverted form in the plot labeled (d). This is the essence of the Log-R correlation method which does, indeed, show evidence of an initial linear relationship (dashed line) with significant departures at higher optical depths as expected. The smooth curves in the final two plots represent analytical representations based on the semi-empirical relationships described in section 5.

6. Example From Multi-trial Analysis (Near IR Band)

In this section, the analysis methodologies are applied to the entirety of the eight trials making up the experiment (tab. 2) using the near IR band as an example. Results for the other bands are presented in appendix C. The purpose in performing multiple trials was to get a good database covering a wide range of optical depths, or "mass loadings," for both obscurant types. The entirety of the experiment was done in as short a time as possible so that the meteorological and atmospheric conditions did not change appreciably. The results for the near IR band are summarized in the plots of figure 9 for all graphite trials and figure 10 for all brass trials.

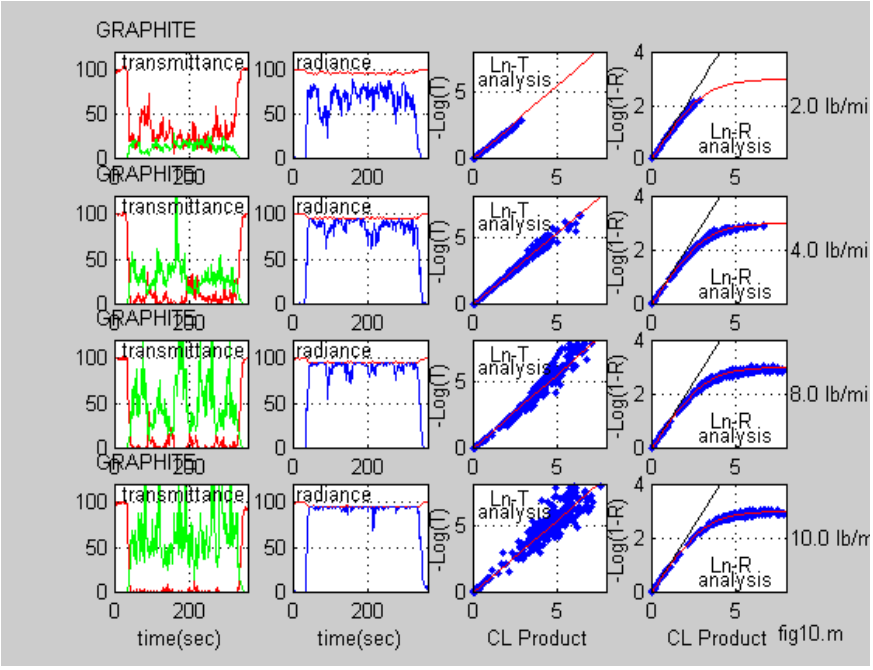

Figure 9. Example of multi-trial analysis for graphite, near IR.

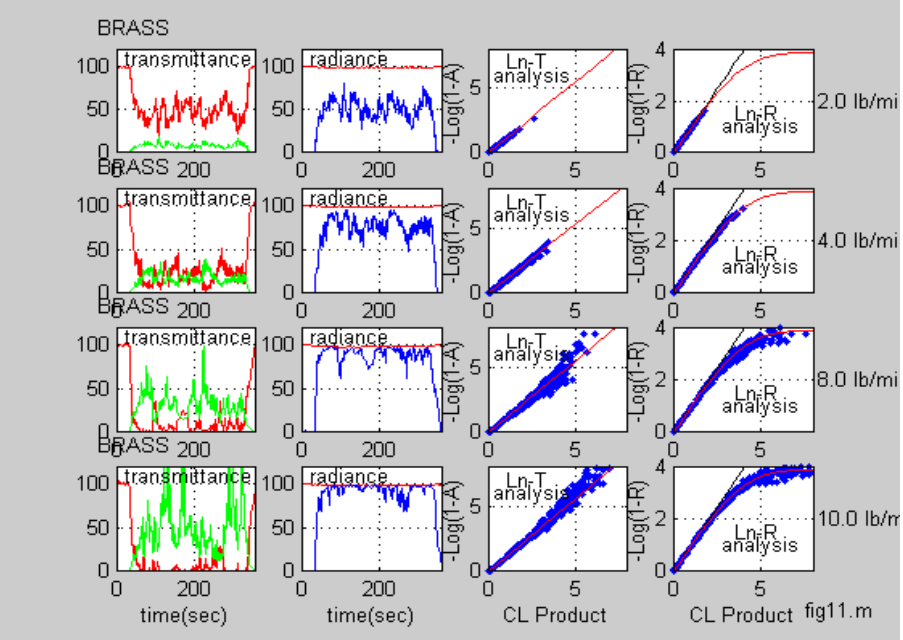

Figure 10. Example of multi-trial analysis for brass, near IR.

In each of the figures, the results are grouped into a 4x4 matrix of plots with the rows and columns defined as follows. The first column in each set represents the measured transmittance plotted as a function of time along with the corresponding optical depth (x10) as determined from the Beer's Law relationship at each time step. In both cases the plots represent the average over the two transmissometer paths. The second column represents the measured total radiance along with the calculated path radiance as determined from eq 8. Both the transmittance and radiance data refer to relative values as determined by normalizing to the clear air readings as discussed in section 4. The remaining two columns represent the results of the Log-T analysis applied to the transmissometer data (third column) and the corresponding results of the Log R analysis applied to the radiometer data (fourth column). In all cases the horizontal rows refer to each of the four generator settings (mass emission rate) as indicated on the margin to the right.

Some insight can be gained immediately from even a casual inspection of the general trends in the various plots. For example, it is clear from examination of the transmittance plots that the optical thickness increases (and consequently the transmittance decreases) with increasing mass loading and the fact that, for the same mass loading, the graphite optical thickness is generally higher than the corresponding value for brass (actually most noticeable at the lower mass loadings). There was some early concern that, at the higher mass loadings, the transmittance may be so low as to exceed the lower threshold of the MPTR system. Evidently this is true for the extreme cases where the transmittance appears to "bottom out" and the optical thickness appears to exceed the upper limit near τ=12. Later it was established that this limit occurred for measurements performed at optical depths exceeding τ=8 which were subsequently ignored in the analysis.

Referring now to the radiance data (second column), it is apparent that the measured total radiance is much less sensitive to mass loading than either the optical thickness or the transmittance. In fact, there is almost no change in the measured value of either the path radiance (lower trace) or the total radiance (upper trace) in the lower three scans for either sample. Another important qualitative observation is the fact that the total radiance is relatively insensitive to the optical depth fluctuations, much unlike either the path radiance or transmittance. The reason for this behavior is, of course, due to the nature of the competition between the direct and diffuse contributions alluded to in previous sections. It is also immediately apparent from the second column that the path radiance is initially higher for graphite (75 percent) than for brass (50 percent) and that both increase with increasing mass loading, quickly reaching a "saturation level" most evident in the extreme rates where the path radiance makes up the near entirety of the total radiance, a fact most apparent in the extreme for graphite.

Turning now to the Log-T analysis results (third column) it is clear that, despite the variations and fluctuations in the raw transmittance measurements, the results of the analysis show a much more ordered view as manifested by the near straight line relationships. The apparent "noise" in the data which generally appears to increase with increasing optical thickness could be due to real world (turbulent-driven) fluctuations but is more likely due to experimental errors often observed in these type experiments when the transmission is very low. For both samples, the results strongly support the Beer's Law formulation as evidenced by the near straight lines in most cases although there is some indication of a "mass loading" effect manifested by a slight increase in slope with increased obscurant rate for optical depths approaching the MPTR limit. Overall, however, the plots are "well-behaved" and tend to verify the initial assumptions concerning the expected obscurant behavior upon which the experiments were based.

Turning next to the Log-R analysis (fourth column), a cursory inspection of the results confirms our earlier findings supporting the linear dependence at the lower optical depths which is apparent in both cases. However, the breakdown of the linear region is also immediately apparent as evidenced by the flattening out of the plots in the "saturation region" at the higher optical depths which is most apparent in the graphite sample. Direct comparison between of the graphite and brass show a difference in the path radiance behavior, most evident in the maximum value attained (~3 for graphite, ~ 4 for brass) and due presumably to the difference in the obscurant optical properties, most likely the single scattering albedo.

To summarize to this point, the results thus far tend to support the underlying theory and, this not necessarily unexpected, for the transmittance measurements which have been the subject of past experiments. The major new surprise lies in the success of the Log-R method in presenting the results in the form of "well- behaved" correlation plots which show major promise as a new tool for quantifying path radiance. Although the conclusions, to this point, are based only on the MPTR near IR measurements, similar results apply for the other bands and are presented either in appendix C or in the section to follow.

7. Results from IR Imagery (Mid- and Far Infrared)

The full set of measurements from the dual band IR imager was not available at the time of this report, but some preliminary data were extracted from the first two trails to more or less corroborate the MPTR results. In this section, an analysis similar to that of section 6 is described using a selected portion from each (time-dependent) frame of the IR imagery. The IR data were collected at a rate of 30 frames per second with each frame consisting of a 320x240 pixel matrix for each of the two spectral bands (i.e., mid-and far IR) and are described in more detail in appendix D. The analysis here applies to the average radiance from a 10x10 pixel area located approximately half way between the transmissometer guide sources which is roughly the same area sampled by the MPRT (cf. fig. 1, appendix D).

A major technical advantage offered by the MPTR is the use of the transmissometer guide sources to determine the cloud transmittance and the subsequent optical depth neither of which are directly attainable from conventional imagery taken alone. Thus the first major task is to determine an accurate method for calculating the (time-dependent) optical thickness for the path corresponding to the selected pixel area. Once this is done, then the path radiance can be calculated from the IR imagery using eq 8, and the analysis can proceed in the same manner as described in section 6.

7.1 Estimation Of Optical Thickness

For the particular situation here, a fortuitous circumstance exists wherein the extinction coefficient, and, hence, the transmittance is (nearly) the same for both the mid- and far IR bands suggesting that a band differencing approach may be accurate and feasible for calculating the optical depth using the empirical relationships of section 5. Stated briefly, the method is to iteratively adjust the optical thickness at every time step so as to simultaneously balance the fundamental relationship of eq 1 for the two spectral bands treated. That is:

$$\text{imagery analysis}: \quad Y_4(\tau,t) - R_4(t) = Y_3(\tau,t) - R_3(t) \tag{15}$$

where, R_3 (t) and R_4 (t), refer respectively to the measured mid- and far IR total radiance obtained directly from the imagery and $Y_3(\tau,t)$ and $Y_4(\tau,t)$ refer to modeled values based on the empirical parameters derived from the MPTR analysis. Equation 15 is solved using iterative methods to find the optimal optical depth at each time step which is then assumed the same for both spectral regions. In practice, the method worked better than expected with the biggest uncertainties being in the inherently ill-conditioned “saturation” region occurring at the higher optical depths.

7.2 Determination of Path Radiance

The results of the frame-by-frame extraction of the IR signal and the corresponding calculated optical depth are shown in figure 11. The plots produced the equivalent of a time scan of total radiance comparable, in principle, to that obtained with MPTR radiometer. In figure 11, the plots on the left refer to graphite, and those on the right refer to brass.

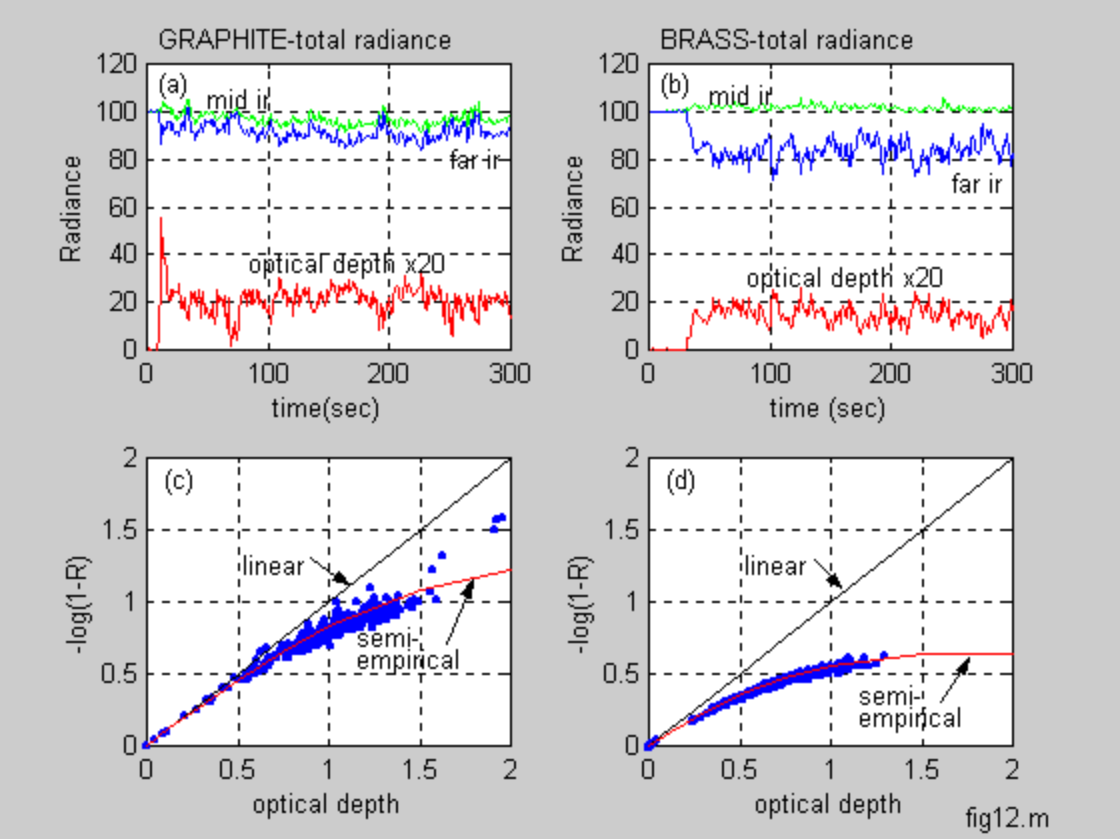

Figure 11. Plots showing results from analysis of imagery.

In figure 11, the upper two plots show time traces of the normalized total radiance for the two bands as obtained in the manner described in section 6 plus the calculated optical depth (shown x10) as determined from eq 15. The lower two plots represent the results of the corresponding Log-R analysis and the subsequent comparison with the semi-empirical expressions.

Looking first at the upper traces in the radiance plots, in all cases, the effect of the obscurant is not necessarily large, resulting at most in a reduction of the total radiance by only 20 percent which occurs for the far IR brass case. It is also evident from the mid-IR results that, upon the introduction of the obscurant, the total radiance decreases slightly for the graphite sample but increases slightly for the brass sample. Both of these observations are in qualitative agreement with the MPTR data although it does appear that the earlier results showed a more marked effect

than those from the imagery. An examination of other pixel areas in the mid-IR imagery confirmed the fact that the total radiance in most cases is less affected by the graphite and, in some cases showing an actual increase when the obscurant is introduced (appendix D). Perhaps the most significant new finding from the imagery to this point is the fact that, for both obscurant types, the total radiance for the far IR band is measurably lower than that for the mid-IR band with the effect being more pronounced for the brass sample than for the graphite sample. This may be due, in part, to the slightly smaller mass extinction coefficient in the far IR band although this alone cannot explain the magnitude of the difference. Another plausible explanation may be based on differences in the obscurant albedos, although any conclusions at this point are risky due to the interacting environmental and obscurant factors identified in the fundamental relationship of section 1 which are all present in the IR bands.

Turning now to the lower plots of figure 11, the Log R method for the far IR again resulted in well-behaved correlation plots with the same characteristic features observed from the MPTR analysis. The linear theory in both cases appears to be valid only for optical depths less than about 0.50 for graphite and only about 0.25 for brass which is a much lower threshold than was observed for the mid IR. There also appears to be more scatter in the graphite correlation plots when compared with brass and this again may be due to differences in the balance between emissive and reflective processes for the different obscurant types as predicted by theory. However, some caution is needed in interpreting the results as some artifacts were found in the imagery due presumable to time lags, and one adjustment on the order of a few seconds was required for the graphite data.

8. Summary and Discussion

From the evidence presented, clearly the MPTR measurements, coupled with the Log-R/T correlation methods, provide a reliable source of data for the experimental determination of both the aerosol transmittance and path emission/radiance. The same statement may be applied to the IR imagery although the results at this point are not conclusive. In this sense, the major object of the experiment was accomplished; however, a number of new findings surfaced in the course of the analysis which are briefly summarized in this section. In the final two paragraphs some of the more significant technical caveats are reviewed and some future requirements are discussed.

8.1 Performance of Semi-empirical Methods

From a modeling point of view, perhaps the most significant finding thus far is that the measured data can be represented by fairly simple semi-empirical expressions that are consistent with the existing theory underlying the ARL COMBIC and PILOT81 methods. It is equally important that the analysis allows for the separation of the purely obscurant effects from the purely ambient effects such that the results can be applied to arbitrary ambient conditions other than those of the experiment, *per se*. This latter point is conveniently summarized in quantitative form in table 3 which gives our best estimates of the semi-empirically derived parameters discussed in section 6. The corresponding semi-empirical mathematical expressions are formed by recasting the equations of section 1 into a slightly more practical form as follows:

transmittance :

$$T_i(t) = exp[-\alpha_i CL(t)]$$

direct radiance :

$$I_{dir}(t) = I_{src} T_i(t) \qquad (16)$$

total radiance :

$$I_{total}(t) = I_{dir}(t) + \{ I_{amb} R_i(t) + I_{cld} E_i(t)$$

where CL(t) is the time-dependent path integrated concentration, or CL Product, which we assume to be known or derived from the analysis. In this expression, the quantities I_{amb} and I_{cld} take the place of the relative parameters a_i and b_i in eq 2 and are assumed known or calculated from the ambient temperatures using eq 4 or some equivalent measurement. Likewise, the quantity, I_{src} is assumed to be a known input representing either the "target" or "background" depending upon the specific application. The remaining unknowns in eq 16 are the obscurant cloud reflectivity and emissivity functions which, in general, can be estimated from first principles using models such as PILOT81, provided that the mass extinction coefficient and albedo are known, or, more accurately, from the semi-empirical relationships of eq 12 and the parameters of table 2 if the obscurant under consideration is one of those tested.

Table 3. Summary of semi-empirical parameters derived from measurements.

a. graphite	α	τ_1	τ_2	β	a_i	b_i
mid ir	1.37	1.00	1.152	0.742	0.750	1.021
far ir	1.31	1.00	0.750	0.387	0.120	0.950
b. brass	α	τ_1	τ_2	β	a_i	b_i
mid ir	0.97	1.00	0.575	0.856	0.750	1.021
far ir	0.95	1.00	0.650	0.542	0.120	0.950

For completeness the first two columns of table 3 lists the best estimates of the obscurant mass extinction coefficient and single scattering albedo which are based either upon the Log R/T analysis or from other sources in the literature. The next three columns are the best estimates of the parameters needed to calculate the emissivity and reflectivity functions using the semi-empirical relationships of eq 12. The final two columns give the best estimates of the environmental parameters (a_i and b_i) that best describe the environmental inputs appropriate for the particular atmospheric conditions experienced during the experiments and are related to the appropriate clear air readings as discussed in appendix B.

8.2 Performance of Log-R/T Correlation Methods of Analysis

In general, the Log-T correlation method worked well in analyzing the MPTR transmissometer measurements. For the most part, all plots consistently produced reasonable linear relationships for all mass loadings and good estimates for the corresponding empirically derived optical constants (tab. 3) which are in general good agreement with theory (i.e., COMBIC) and with experimental findings from other studies. Likewise, the analogous Log-R correlation method

worked well in analyzing the MPTR radiometer measurements. In particular, the path radiance results at the smaller optical depths exhibiting the expected linear behavior, and the results at the larger optical depths exhibited large deviations due to higher order effects that are generally consistent with theory (i.e., PILOT81). The exercise using the dual band "Delta R" method for estimating optical depth (eq 15) from the IR imagery offers a significant technical improvement over the linear method and was surprisingly successful, but preliminary.

8.3 Relationship to the Sky-to-Ground Ratio

One of the most important parameters used to model the effects of target-background contrast and the consequent effects on military systems is the so-named sky-to-ground parameter, which is a key input in tactical wargame simulations such as CASTFOREM and discussed in detail in the older literature (*9*). Although there have been numerous concept papers written on the importance of obscurant-induced contrast effects, there is little direct data on quantitative field measurements comparable to the study here. As it turns out, the normalized path radiance as defined here can be used to determine other obscurant parameters such as the target-background contrast and contrast transmission and is thus entirely equivalent to a sky-to-ground parameter measurement. This is shown by starting with the usual definition of target background:

$$\text{contrast}\, C(\tau) = \frac{I(\tau_{tgt}) - I(\tau_{bkg})}{I(\tau_{bkg})} \tag{17}$$

which can be evaluated immediately by applying eq 1 of the main text twice, once for the target-receiver path and once for the background-receiver path accounting for the total radiance in each case. That is:

$$C(\tau) = \frac{I_{tgt}(o)[T(\tau_{tgt}) + S(\tau_{tgt})] - I_{bkg}(o)[T(\tau_{bkg}) + S(\tau_{bkg})]}{I_{bkg}(o)[T(\tau_{bkg}) + S(\tau_{bkg})]} \tag{18}$$

where, as in all cases throughout, T(τ) is the aerosol transmittance and S(τ) is the normalized total path radiance.

It is usual in applications to assume that the two paths (target and background) are nearly coincident so that the following approximations apply:

$$\begin{aligned} T(\tau_{tgt}) &\approx T(\tau_{bkg}) = T(\tau) \\ S(\tau_{tgt}) &\approx S(\tau_{bkg}) = S(\tau) \end{aligned} \tag{19}$$

which, upon following through in eq 18, leads to a cancellation of the path radiance terms in the numerator and a subsequently less involved expression. That is, after some rearranging:

$$C(\tau) = \left[\frac{I_{tgt}(o) - I_{bkg}(o)}{I_{bkg}(o)}\right]\left[\frac{T(\tau)}{T(\tau) + S(\tau)}\right] \tag{20}$$

where the first term in square brackets is called the intrinsic (or unobscured) target-background contrast, and the function in the second set of brackets is called the contrast transmission which

is formally defined as the ratio of the (obscured) contrast to the (unobscured) contrast. That is, defining C(o) as the intrinsic contrast and substituting the exponential form for transmittance, results in:

$$C(\tau) = C(o)\{\frac{1}{1 - S(\tau)/T(\tau)}\} \tag{21}$$

which is identical to the usual expression if S(τ) is identified with the sky-to-ground parameter.

It should be remarked that the origin of the sky-to-ground ratio terminology traces to the treatment of clear air scenarios and a semi-infinite plane layer atmosphere applied along a horizontal path in which case the Beer's Law expressions are adequate. The extension here, however, represents the more general case making the associations with the sky and the unqualified usage of the Beer's Law somewhat misleading to the uninitiated reader.

8.4 Limitations of Linear Models-Path Radiance

The results of the Log-R correlation analysis discussed in the various figures of section 5 clearly demonstrate the limitations of the linear approximations in accurately modeling path radiance, especially at the higher optical depths. The usage of such models to determine optical thickness from radiance measurements is also inaccurate and misleading, especially in the saturation region identified in figure 11. However, a quick dismissal of such models as a valid approximation is somewhat premature for reasons that will be made apparent later in this section. To illustrate the results are re-examined using the example of figure 12 as a reference.

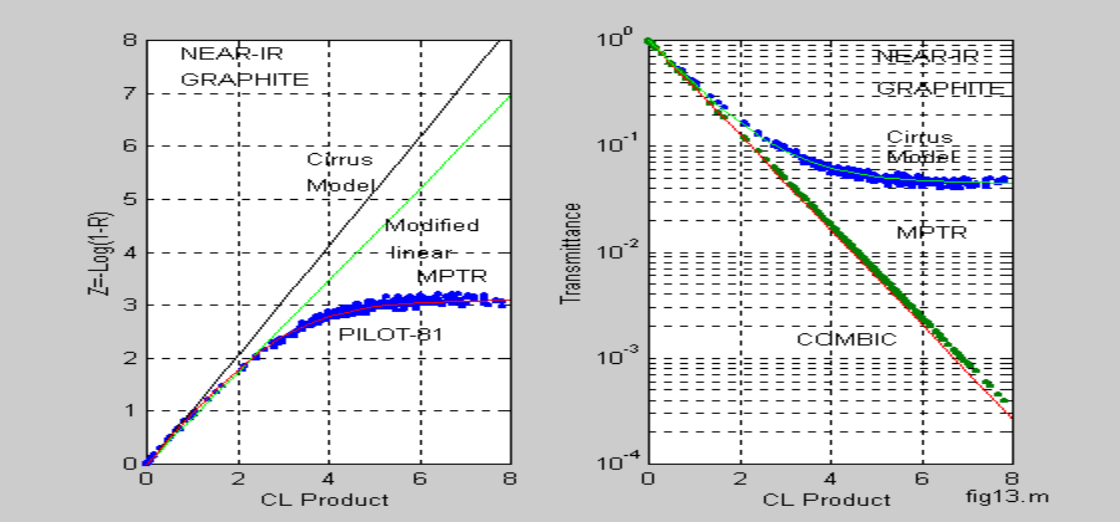

Figure 12. Example comparing linear models with theory.

The plot on the left was produced using the Log-R method as described in section 7 as applied to a typical graphite trial using the near IR measurements. As usual the path radiance data plots are characterized by an initial linear region followed by a transition to the "saturation" region where the plots tend to a constant value as the cloud becomes optically thick, much in the manner predicted by PILOT81 (fig. 6). The Cirrus model represented by the upper straight line in Fig. 12 is reported to be derived from single scattering and is included here at the request of the

SCIMITAR group (*10*). The lower straight line represents a limit that is referred to as the "modified linear" region.

The example here demonstrates the limitations of models based on the linear approach although it is clear that the performance can be improved significantly by adopting the modified empirical method suggested in figure 12. However, the real significance of this example is that the linear region extends up to an optical depth of about τ=3 which is surprisingly larger than might be expected. The case for brass in the visible band (fig. 3, appendix C) is even more surprising in that the linear region extends up to almost τ=8. On the other hand, for brass in the far IR (fig. 12) the linear region extends up to only about τ=0.50. In the following paragraphs these findings are examined in light of the more general theory underlying the PILOT81 model.

The fact that the plots are initially linear is not necessarily unexpected, and this observation might be interpreted (although not necessarily so) as an indication of the predominance of single scattering. Although this latter statement is true, it can be misleading because there are a number of other situations where a linear form is theoretically predicted. To understand why this "unexpected" linear behavior might be happening consider that there are at least four other common situations wherein the theory predicts linear behavior even in the multiple scattering and emission regime. The first obvious case is the situation where the source function is essentially constant over the path of propagation which was already discussed in connection with eq 12. This is the situation commonly modeled in clear air scenarios for horizontal propagation through plane parallel layers that historically lead to the development of the sky-to-ground parameter. Another "obvious" situation is the case of temperature equilibrium which occurs when the ambient input radiance is equal to the cloud blackbody radiance (i.e., when a_i=b_i) in which case, according to eq 10, the path radiance expression reduces to the linear form. The third case occurs for the extreme of conservative scattering (i.e., ω=1) which is apparently the situation noted earlier for brass. The fourth situation occurs for the extreme of total absorption (i.e., ω=0) in which case all multiple and single scattering contributions are zero, and the linear form is strictly applicable. It is interesting that the results from the experiments suggest that some of these conditions are not far from those that actually were experienced during some of the field trials.

8.5 Limitations of Linear Models-Transmittance

The results thus far are encouraging in the sense that the linear model may often be a good approximation for modeling path radiance from the known optical thickness, even in cases where there is strong emission and multiple scattering. On the other hand one must proceed with more caution when dealing with the inverse application to determine the optical depth from radiance measurements as is sometimes attempted with field imagery. The reason for caution is clear from casual inspection of the saturation region in the Log-R plots wherein the path radiance attains a constant value independent of any changes in the actual optical thickness. This "ill conditioning" of the process can be demonstrated by examining the error, $\Delta\tau$, introduced in using the linear approximation, that is:

$$\Delta\tau \approx \tau - Ln[1 - S(\omega;\tau)] \tag{22}$$

where, τ, represents the actual measured optical depth and the second term represents the expected error, which is immediately recognized as being identical to the argument, Z(t), used in the Log-R method of eq 14. Thus the magnitude of the error can be read directly from fig. 12 as the difference between the linear model curve and the corresponding data points. This is demonstrated in fig. 12b which demonstrates the error introduced by using the linear approximation to calculate transmittance solely from radiance measurements. It is immediately clear that the linear method is adequate for small optical depths but the error grows rapidly beyond the linear threshold and ultimately exceeds two orders of magnitude at the extreme, thus seriously under-predicting sensor performance. Unfortunately, much of the data of record from the Smoke Weeks apply to the saturation region where the largest uncertainties occur. This situation was, of course, not unanticipated here and was motivation for using the MPTR system and for designing the experiment to cover a wide range of light to heavy mass loadings.

8.6 Caveats and Comments

The review of results and the various cross-checks suggest that the experiment was successful in obtaining an accurate and reliable database on the simultaneous measurements of path radiance and optical thickness for a wide range of obscurant mass loadings. On the other hand, there are a number of caveats that need to be addressed, the first is that the measurements were all obtained over a single set of horizontal paths and over (near) constant ambient conditions and, thus, some caution needs to exercised in extending to more universal scenarios. However, the manner in which the analysis was conducted to separately extract weather dependent and obscurant dependent parameters allows for scaling of the results over a wide range of ambient conditions as implied in eq 16. This hypothesis is based on good theoretical grounds but has not necessarily been tested with real data.

The second caveat is that, in performing the analysis the implicit assumption of isotropic scattering was also made but this assumption also was not tested directly. In practice, this means that somewhat different results might be expected if different viewing angles were used and this would be especially important at the shorter wavelengths and thinner optical depths where angular dependent solar in-scattering is most significant. Such details can be addressed with modeling but are difficult to verify in the field due to the inordinate difficulty in measuring all of the necessary inputs. These details are quantitatively important but probably do not alter most of the broader qualitative information derived from the experiments.

The third caveat involved scaling the results to higher (or lower) values for the environmental inputs (i.e., eq 16). All input radiative sources were implicitly assumed to be isotropic and for the obscurant cloud to be isothermal. Again, these assumptions do not necessarily reflect on the capability of the models but are more a matter of practical concern in the difficulty in actually measuring all possible inputs accurately. However, based on the *a posteriori* results, no direct evidence shows that a more accurate characterization of the ambient inputs would change any of the major conclusions. Finally, the assumption that the cloud is isothermal is probably not serious for the experimental situation here because the aerosol generation process does not heat the cloud much beyond the ambient, and, thus, details of the cloud temperature structure are of lessened significance.

8.7 Future Requirements

Besides the usual problem of trying to quantitatively extend the findings to arbitrary scenarios of the real world which itself is "unquantifiable" in a practical sense, there are a number of more realizable goals for the immediate future. The first requirement is to validate the thermal imagery data using some of the same techniques and relationships as used here for the MPTR. Our experience (somewhat limited) with the IR imagery (appendix D) suggests a new method for extending the analysis to the spatial regime and techniques that may eliminate the bias in estimating the optical thickness from imagery. A more practical requirement is to exploit the fact that we have produced a method for obtaining a near direct measurement of the traditional sky-to-ground parameter needed by the user community.

Other more esoteric requirements involve the analysis of the statistical relationship between the directly transmitted signal and the interfering path radiance signal. These two quantities seem to correlate quite well in some applications and not so well in other applications and may explain some of the scatter in the correlation plots. From a theoretical standpoint this is a problem that needs to be addressed using a stochastic modeling approach which was more or less avoided in the analysis thus far. There are also practical applications for developing this type of analytical approach for synthetic scene development for future systems analysis where the requirements on accurate statistical renderings are of increased significance. From a practical viewpoint, two immediate follow-on experiments are evident. The first is to repeat the experiments during nighttime so as to eliminate the effect of solar loading and thus the measurements would lend more accurate information on the aerosol emissivity. The second is to include a set of experiments with the obscurant heated to a temperature that may be several (or even several hundred) degrees higher than the ambient temperature. Such strongly emissive conditions are expected to affect IR sensor performance, and the need for accurate modeling for this case has been pointed out by the user community. It was, in fact, this latter deficiency that lead to the development of the PILOT81 model and was a prime motivator in performing the analysis of the experimental data.

9. References

1 Sutherland, R.A., "Determination and use of IR band Emissivities in a Multiple Scattering and Thermally Emitting Aerosol Medium", ARL Technical report, in review.

2. Wetmore, A. and S.D. Ayres, "COMBIC-Combined Obscuration Model for Battlefield Induced Contaminants", US Army Research Laboratory Technical Report, ARL-TR-1831, August 2000.

3. de Jong, A.H.,1984, "Results of NL Transmission and Emission Measurements during Smoke Week VB and VI, Proceedings of Smoke Symposium VIII, April, 1984.

4. Hoock, D.W. and R.A. Sutherland, 1993, (Obscurant Countermeasures), Chapter 7 in the EO/IR Handbook, published by SPIE, Bellingham, WA.

5. Kuhlman, M.R., et. al., 1995, "Evaluation of Physical Properties of a Foreign Smoke" FMTR-1620-90030-001-94, prepared for National Ground Intelligence Center, August 1995.

6. Anderson, L., Chenault, T., Churchman, J., Hornack, R. and T. Smelker, 1999, "Scene and Countermeasure Integration for Munition Interaction with Targets", U.S. Army Research Laboratory Technical report, ARL-TR-1633, September 1999.

7. Gillespie, P.S.,1995, "TARGAC Technical Description and User's Guide", U.S. Army Research Laboratory Technical Report, ARL-TR-273-3, April 1995.

8. Mackey, D.C., Dixon, D.S., Jensen, K.G., Loncarich, and J.T. Swaim,1992, "CASTFOREM (Combined Arms and Support Task Force Evaluation Model) Update: Methodologies", Department of the Army Technical Documentation, TRAC-WSMR-TD-92-011.

9. Seagraves, M.A. and J.M. Davis, 1989, "Target Acquisition Tactical Decision Aid Software Technical Documentation", ASL-TR-0252, September 1989.

10. Chenault, T., Equation of the form $P=J(1-e^{-t})$, Cirrus computer program, unpublished.

11. Lopez, C. and R.A. Sutherland, 2002, "Software Methods for Imagery Analysis", U.S. Army Research Laboratory Technical Note, in preparation, December 2002.

Appendix A. MPTR Theory

In the basic transmissometer configuration, the raw signal is generally assumed to be comprised of the following contributions, including signal, noise, and interference components of various origin:

$$
\begin{aligned}
S_{dir}(\Delta\lambda_i) = R_{sys}(s)\{[(I_{src} + I_{bkg})e^{-(\tau_{aer}+\tau_{atm})}] &\text{.....direct transmittance} \\
+ [I_{src} f_{dir}(\delta\omega,\tau) + I_{bkg} f_{bkg}(\delta\omega,\tau)] &\text{.....forward scatter} \\
+ [I^*_{ems}(\tau_{aer}) + I^*_{sct}(\tau_{aer})] &\text{.....path radiance, aerosol} \\
+ [I^*_{ems}(\tau_{atm}) + I^*_{sct}(\tau_{atm})] &\text{.....path radiance, atmosphere} \\
+ N_{atm}\} + N_{sys}(s) &\text{.....noise, atmsophere \& system}
\end{aligned}
\tag{A1}
$$

In eq A1, the quantity labeled $R_{sys}(s)$, is the system response function that converts the optical signal (s) to a voltage signal (S_{dir}) and is usually assumed to be a linear function for signal levels in the region of practical interest; although this assumption can break down at very high signal levels called the saturation region. In eq A1, the total path optical thickness includes contributions from both the smoke aerosol, t_{aer} , and the intervening atmosphere, τ_{atm}, which taken together make up the total path optical thickness ($\tau=\tau_{aer}+\tau_{atm}$). Also, in eq A1, the first term inside the curly braces represents the totality of any directly transmitted radiance and can include contributions from both the transmissometer source, I_{src}, plus any "spill over" from the background, I_{bkg}, within the receiver field of view. The second term represents any contribution due to forward scattering within the field of view, $\delta\omega$, of the transmitter-receiver optical path. Most transmissometer systems are designed such that:

$$I_{bkg}(\Delta\lambda_i) << I_{src}(\Delta\lambda_i) \tag{A2}$$

where acknowledgment of the fact that both the background and source intensities are dependent upon the particular bandpass (Δ_i) under consideration. Thus, from eq A2 it is clear that the background terms can be neglected in comparison with the (very intense) artificial source terms, a condition that greatly simplifies the expression for practical applications.

The third and fourth terms in eq A1 arise from either thermal emission, $I^*_{ems}(\tau)$, or in-scatter from the surroundings, $I^*_{sct}(\tau)$, either from the smoke aerosol, $I^*(\tau_{aer})$, or the intervening atmosphere, $I^*(\tau_{atm})$. In, the usual transmissometer configuration, the source beam, I_{src}, is optically modulated with a mechanical chopper at the transmitter aperture to create an alternating current (ac) signal which is synchronized to the receiver electronics. The signal is then synchronously detected at the chopper frequency (usually around 1000 Hz) in such a way that any direct current (dc) component such as that due to a constant background is not sensed. This method of detection will eliminate most of the path radiance term, thus for all practical purposes the radiance terms are not measured. Therefore for the modulated signal that the transmissometer system actually "sees", eq A1was replaced with the following more simplified form:

$$S_{mod}(\Delta\lambda_i) = R_{sys}(s)\{I_{src}[e^{-(\tau_{aer}+\tau_{atm})} + f_{dir}(\delta\omega,\tau)] + N_{atm}\} + N_{sys} \quad \text{(A3)}$$

where the condition of eq A2was accounted for by ignoring the terms involving I_{bkg} and by using the subscript "mod" to distinguish from the direct signal. For an ideal instrument, the forward scattering term can be minimized by using narrow beam receiver optics and collimated transmitter beams. For obscurants comprised of particles very much larger than the wavelength, the forward scattering lobe is very narrow and very concentrated and can even dominate the signal; however, for the types obscurants used here, the effect is generally negligible. The remaining noise terms in eq A1 represent both optical and electronic noise originating either from the intervening atmospheric path, N_{atm} or purely from the system hardware, N_{sys}. In practice neither of these terms can be completely eliminated but can be accounted for, in the mean, such that:

$$\begin{aligned} &..... < N_{atm}(t) >= 0 \\ &..... < N_{sys}(t) >= 0 \end{aligned} \quad \text{(A4)}$$

where the symbol <X(t)> is used to denote a (short term) average with respect to time. Thus the mean level of noise can be eliminated; however, fluctuations about the mean are almost always present in the field data.

The basic radiometer configuration is similar to the transmissometer configuration except that the artificial optically chopped light source is eliminated thus leaving only the natural background for the clear air source. Also, the forward scatter component in this case forms an authentic contribution to the path radiance since I_{bkg} is from a natural ambient source and, along this same line of reasoning, the atmospheric-induced noise contribution is a bona fide component of the atmospheric source function. Thus in the radiance mode, eq A3is replaced with the following expression:

$$\begin{aligned} S_{rad}(\Delta\lambda_i) = R_{sys}(r)\{ & I_{bkg}e^{-(\tau_{atm}+\tau_{atm})} \\ & + I^*_{ems}(\tau_{aer}) + I^*_{sct}(\tau_{aer}) \\ & + I^*_{ems}(\tau_{atm}) + I^*_{sct}(\tau_{atm}\} \\ & + N_{sys}(r) \end{aligned} \quad \text{(A5)}$$

where, in this case, $R_{sys}(r)$ is the system response function for the radiometer receiver and $N_{sys}(r)$ is the corresponding radiometric system noise.

In the following paragraphs, the assumption is that either eq A3 or eq A5 represents the relationship between the received optical signal and the system output for the transmissometer and radiometer modes respectively. It will turn out that the situation can be simplified even further by "normalized" the signals to their clear air readings which has the effect of eliminating the system response function, R_{sys}, which "cancels" out. It is necessary, however, that the response function be linear in order for this to be valid.

Thus, provided that all sources of error have been kept at a negligible level , then the net result of the data processing procedure should yield a measurement very nearly equal to the aerosol transmittance. That is, assuming S_{min} to be zero (on average) for the calibrated signal and

realizing that S_{max} refers to the clear air transmittance (mean=100%), we have from eq A5, for the ideal case:

$$T_{rel}(\Delta\lambda_i,t) = \frac{R_{sys}(s)I_{src}[e^{-(\tau_{aer}+\tau_{atm})} + f(\delta\omega,\tau_{tot})]]}{R_{sys}(s)I_{src}[e^{-(\tau_{atm})} + f(\delta\omega,\tau_{atm})}$$
$$\ldots\ldots\ldots\ldots\ldots \approx \frac{e^{-(r_{aer}+\tau_{atm})}}{e^{-\tau_{atm}}} = e^{-\tau_{aer}}, \text{for } \delta\omega \to 0 \qquad \text{(A6)}$$

which implies that the relative reading so normalized is a good estimate of the aerosol transmittance provided that the forward scattering contribution is negligible; an assumption that was later tested with the *a posteriori* data.

With the data so calibrated and again assuming the noise terms to be eliminated and noting that S_{max} again refers to the clear air case, and proceeding in a manner similar to that leading to eq A6, the radiometric mode is:

$$R_{rel} = \frac{I_{bkg}e^{-(\tau_{aer}+\tau_{atm})} + [I^*_{aer}(\tau_{aer}) + I^*_{atm}(\tau_{atm})]}{I_{bkg}e^{-\tau_{atm}} + I^*_{atm}(\tau_{atm})} \qquad \text{(A7)}$$

which, in this case represents the ratio of the total (direct + diffuse) radiance to the pre-event clear air total radiance. In most field tests, the atmospheric contribution is kept small by conducting the trials only under clear air conditions in which case, assuming a near horizontal path, we have:

$$J(\tau_{atm}) = J_o(1 - e^{-\tau_{atm}})$$
$$\ldots\ldots\ldots \approx 0;\ldots\text{for} \quad \tau_{atm} \to 0 \qquad \text{(A8)}$$

where J_o is a constant less than or equal to unity depending upon the obscurant albedo and is referred to as the atmospheric optical source function. Inserting this approximation for $J(\tau_{atm})$ in the limit and assuming $[\exp(-\tau_{atm})\sim 1]$, after some minor rearrangement and cancellation, the following expression analogous to the final form of eq A6:

$$R_{rel} = \frac{I_{bkg}e^{-\tau_{aer}} + I^*_{aer}(\tau_{aer})}{I_{bkg}}$$
$$\ldots\ldots\ldots = T(\tau_{are}) + S^*_{aer}(\tau_{aer}) \qquad \text{(A9)}$$

where the first term on the right is the direct transmittance which can be independently calculated from the transmissometer mode measurement, and the second is an additional contribution brought about by the inclusion of the path radiance and can be thought of as a normalized, or relative, path radiance. That is:

$$S^*_{gr}(\tau) = \frac{I^*_{aer}(\tau_{aer})}{I_{bkg}} \tag{A10}$$

which is also referred to as the sky-to-ground ratio discussed in the main text. Thus the MPTR system provides all of the information needed to account for the two major obscuration parameters used in sensor performance modeling.

Appendix B. Clear Air Constants

In executing the experiments, an effort was made to complete the entire set of trials as quickly as possible so as to avoid any problems associated with variations in the atmospheric conditions which could influence the clear air readings. In this section, the values of the clear air readings obtained along the three main sampling paths as measured near the beginning of each trial are documented.

The data in table B1 refer to a the original 12-bit digital readings, or counts, which are assumed proportional to the incoming radiant signal. Inspection of the table values indicates that the most significant variations were in the visible band readings where differences were as high as 30 percent. On the other hand, the near IR readings were the most consistent with differences no higher than 5 percent or so. The effect of the variations here are, of course, strongly mitigated by the fact that independent calibrations were performed prior to each event, thus avoiding any large error.

Table B1. MPTR Clear Air Normalization Constants.

(a) Transmissometer

Trial→	**21601**	**21602**	**21603**	**21604**	**21605**	**21606**	**21607**	**21608**	**21609**
LOS-1									
Visible	2382	1975	2102	2942	2964	2695	2950	2118	2978
Near ir	3722	3730	3728	3769	3804	3864	3579	3575	3728
mid ir	3095	3066	3048	3036	3051	3049	3049	3046	3053
Far ir	2887	2861	2749	2649	2700	2756	2657	2636	2614
LOS-2									
Visible	2236	1531	1746	2532	2527	2077	2418	1770	2514
Near ir	3291	3334	3308	3339	3331	3334	3254	3304	3358
mid ir	2585	2606	2620	2615	2597	2574	2597	2600	2616
Far ir	2875	2633	2613	2565	2548	2609	2631	2576	2621

(b) Radiometer

Trial→	21601	21602	21603	21604	21605	21606	21607	21608	21609
LOS-0									
Visible	2678	2692	2708	2731	2742	2750	2770	2779	2790
near ir	2196	2200	2204	2209	2210	2210	2215	2216	2218
mid ir	1999	1937	2115	1979	2064	1988	2119	2059	2053
far ir	1970	0844	1896	1814	1942	1750	2151	1871	1808

Appendix C. Multi-Trial Summary

Presented in this section, is the remainder of the results from the multi-trial analysis discussed briefly for the single set of near IR results for both graphite and brass presented in section 6. Figures C1–C4 present the remainder of the results for visible and mid-IR bands in the same format as that used in figures 9 and 10.

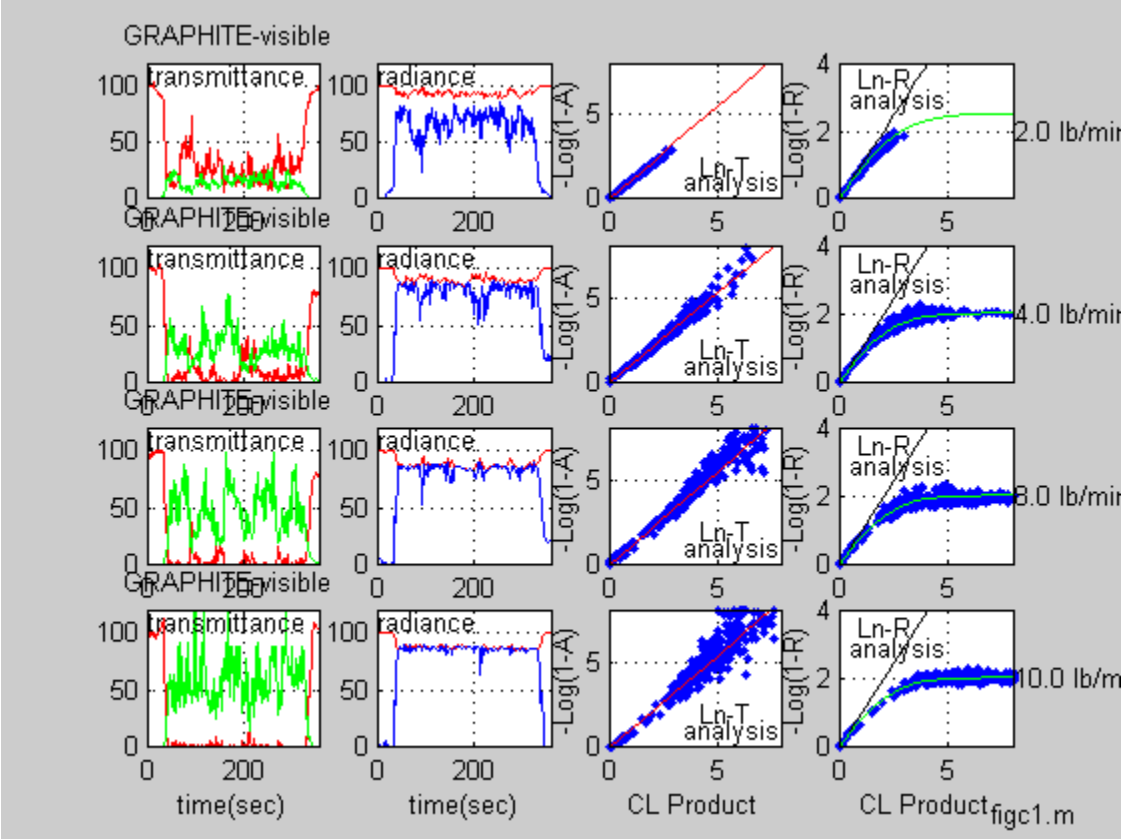

Figure C1. Multi-trial summary, graphite-visible.

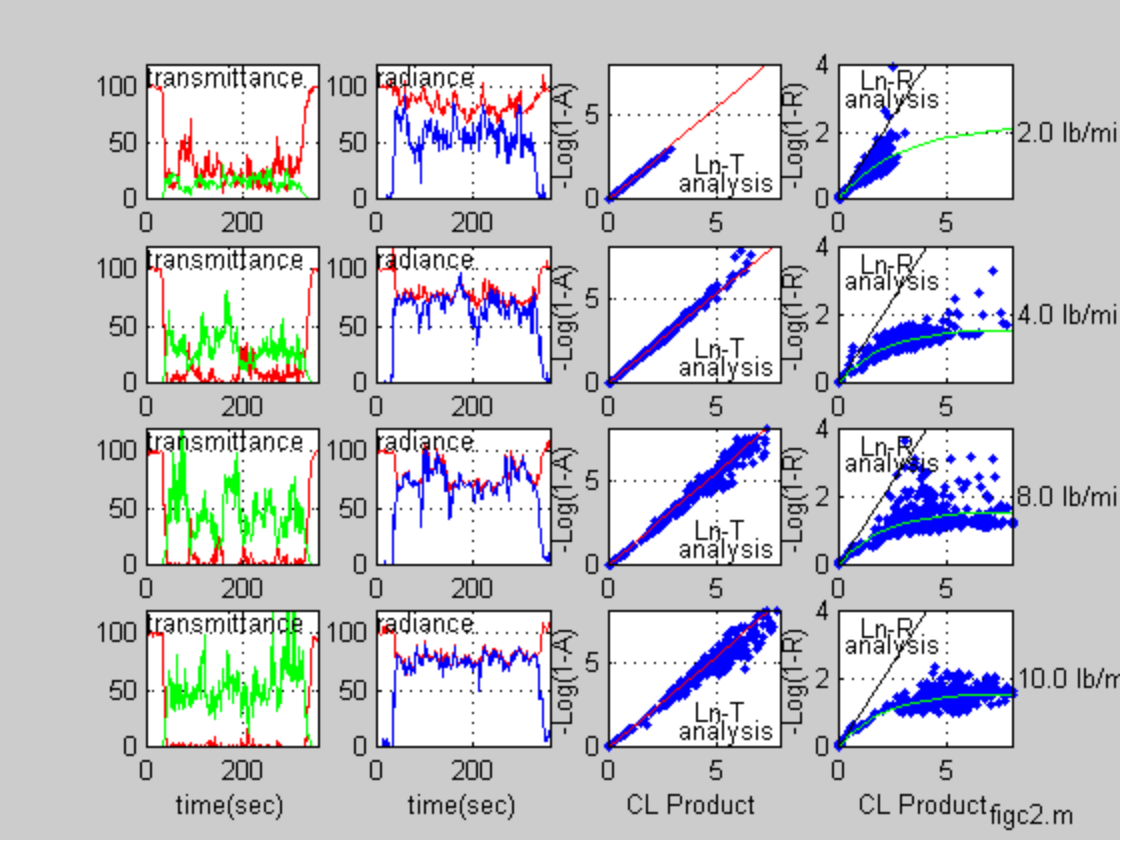

Figure C2. Multi-trial summary, graphite mid-ir.

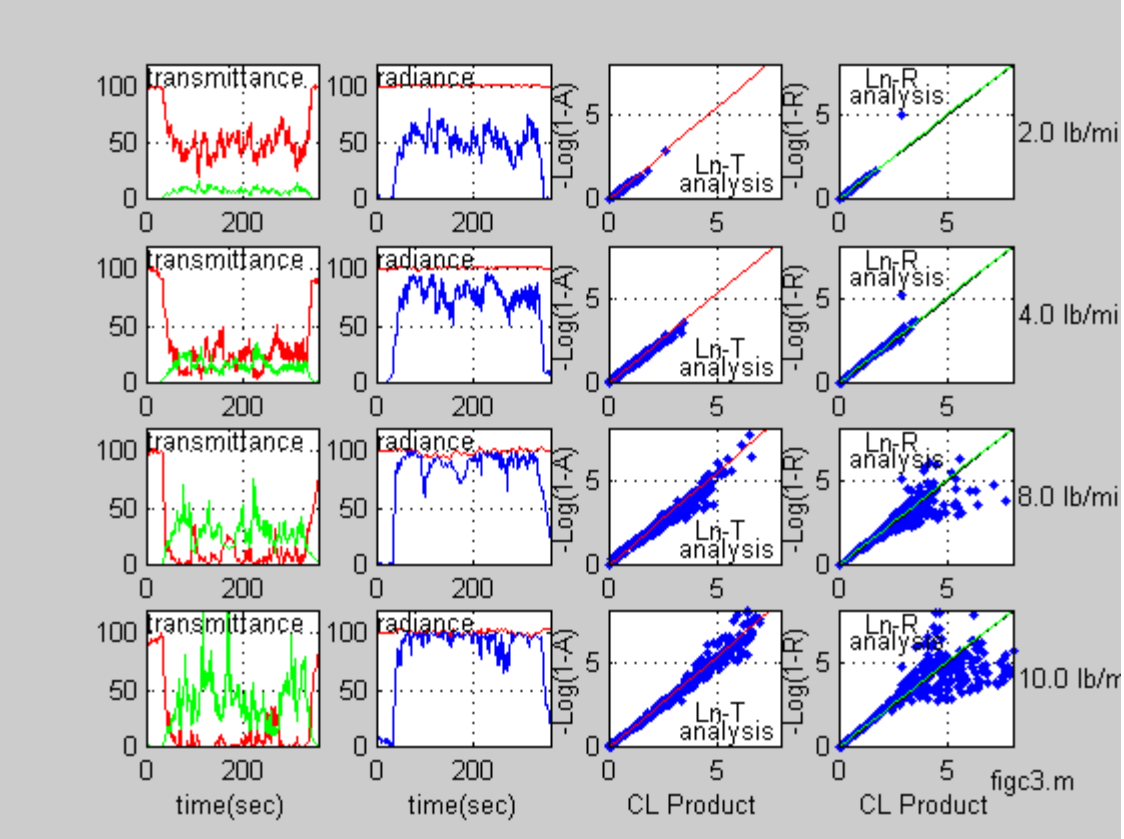

Figure C3. Multi-trial summary, brass-visible.

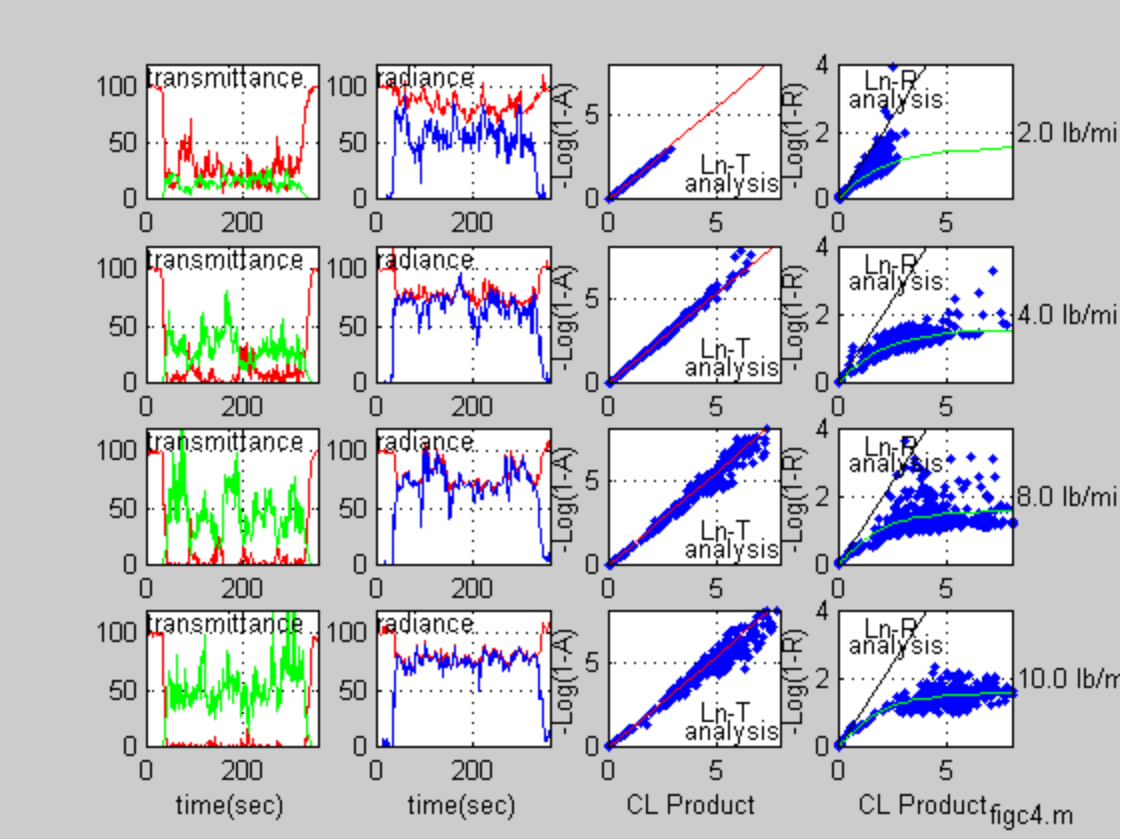

Figure C4. Multi-trial summary, brass mid-ir.

It is reasonably clear from examination of either of the transmissometer correlation plots that the experiments yielded consistent and well-behaved results. This is particularly clear from the third column representing the transmittance correlation plots which are, in all cases, produced highly convincing evidence of linear relationships as predicted by theory. There are, however, some indications of an upward curvature trend in the plots being most noticeable at the higher mass loadings which may be due to effects beyond the scope of the present study. It is also apparent that the scatter in the plots tends to increase with increasing optical depth which is to be expected because of the smaller signals involved.

The results from the path radiance correlation plots are also consistent and well-behaved in that all show a initial linear trend, consistent with the Beer's Law of attenuation, in the thin layer region but with significant departures at higher optical depths and eventually approaching the classical limit in the extreme at the higher mass loadings. A most interesting exception is shown for the case of brass in the visible band which exhibits the linear trend throughout the full range of optical thickness.

Appendix D. Multi-Pixel Data From Ir Imagery

In the main text, the use of the dual band IR imagery data was limited to only a few pixels mainly for the purpose of verifying the MPTR results. However, we do have plans to extend the analysis into the spatial regime using the IR imagery. Some of our preliminary findings suggest that a pixel by pixel analysis of the time scans such as those discussed in section 7 may offer advantages beyond those obtained using conventional imaging analysis tools. The method of sampling the IR imagery is demonstrated in figure D1 (*11*).

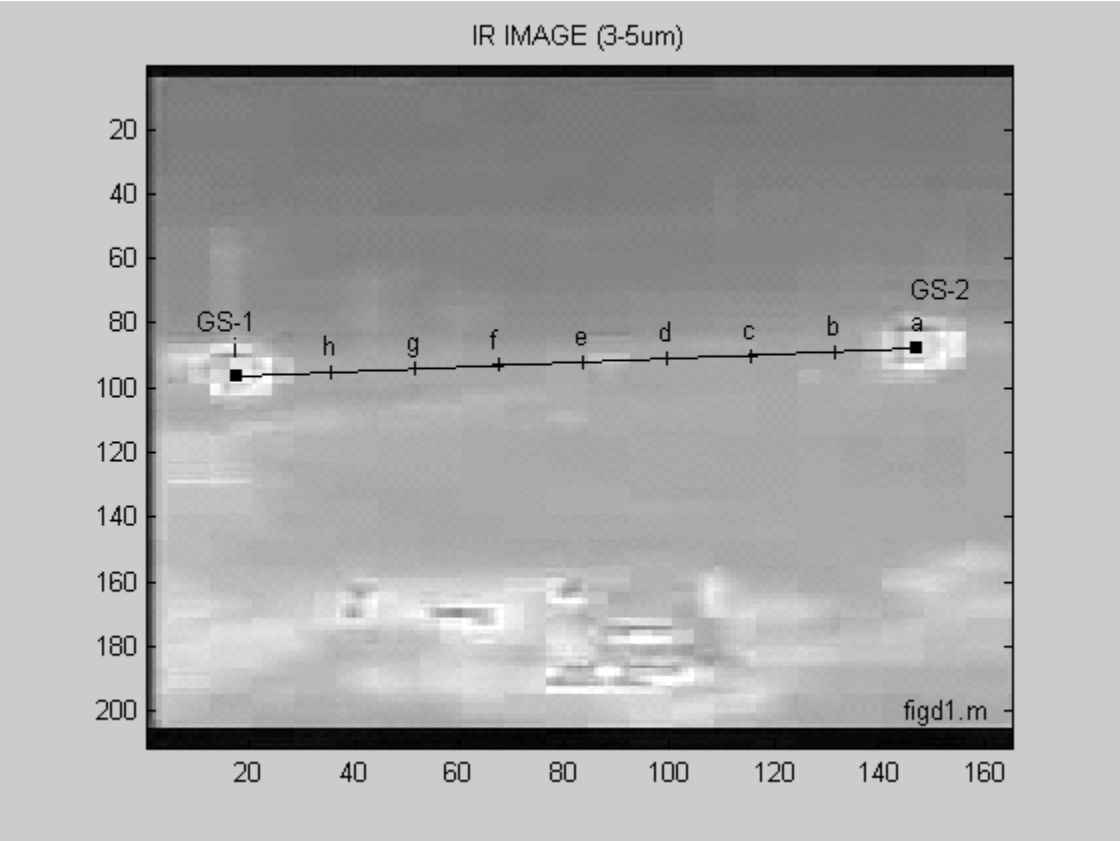

Figure D1. Photograph of single data frame from IR imager.

The photograph of figure D1 represents a single frame taken from the mid-IR imagery file and represents a roughly 320x240 pixel area scanned at a rate of 30 frames per second. The task in this section was to sample the imagery at each of the nine discrete points labeled a through i for each time step and thus produce a time trace of total radiance similar to those of figures 9 and 10.

The results for both the mid- and far IR bands are shown in figure D2 (graphite, trial 21608) and figure D3 (brass, trial 21609).

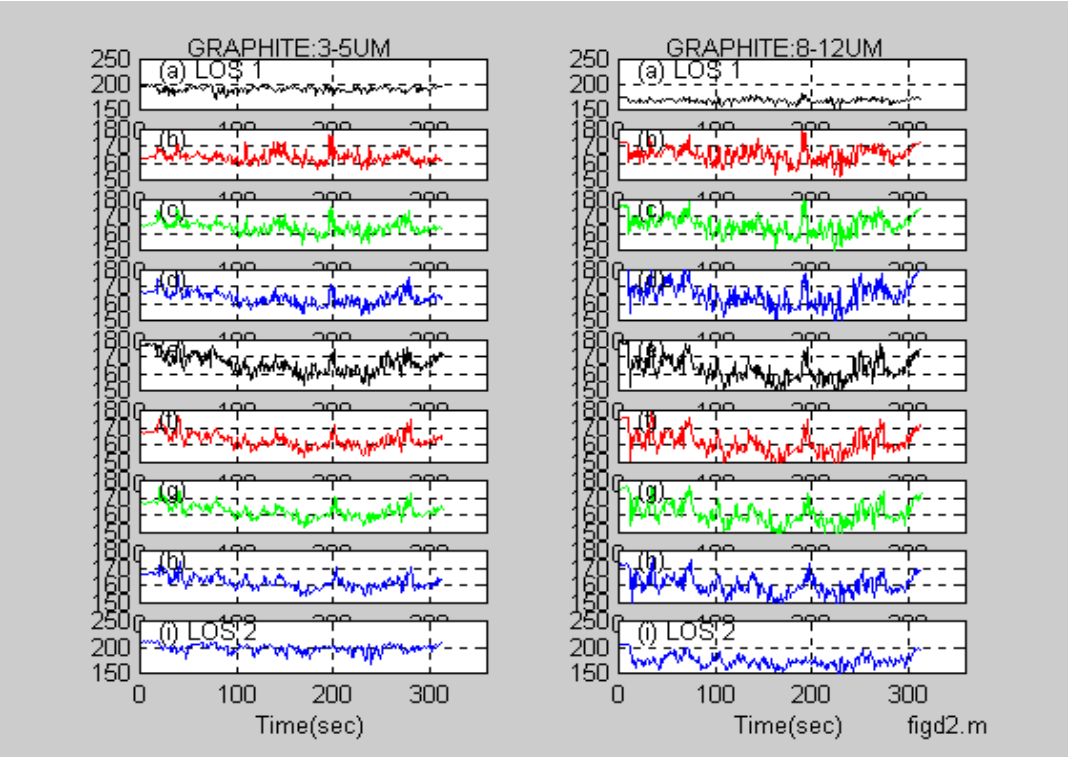

Figure D2. Dual band multi-pixel time scans of total radiance for graphite.

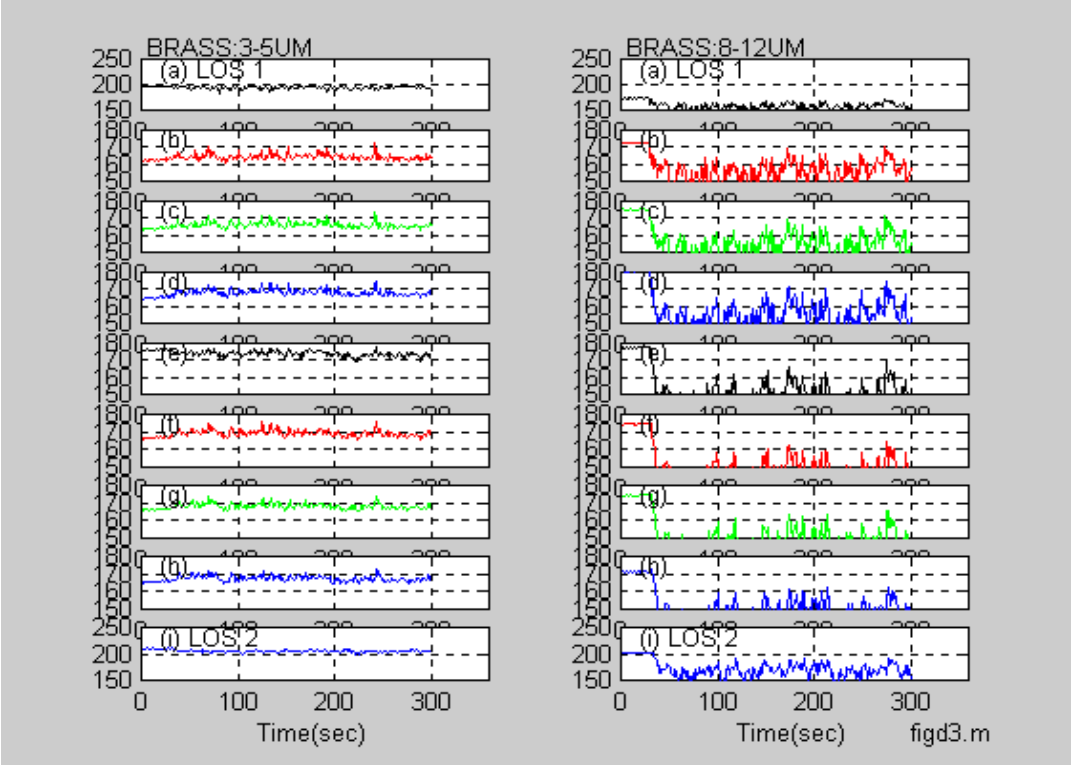

Figure D3. Dual band multi-pixel time scans of total radiance for brass.

In each of the figures, the two distinct columns refer either to the 3–5 um band or the 8–12 um band as noted. Note also that both the extreme upper and extreme lower scans in all cases correspond to paths terminated by the tranmissometer sources and are thus much more intense than the others which are terminated by the natural background, whatever it may be.

Several things are immediately apparent from even a causal inspection of the plots. First, for the mid-IR band, the net effect of the obscurant is not large especially for the case of brass whereupon the total radiance, in most cases, actually increases when the obscurant is introduced as was observed earlier. On the other hand the effect of the obscurant on the far IR band is much more pronounced and more so for the brass example where the traces actually "bottom out" at the lower threshold. This too was noted in the earlier discussions of Section 9. Another interesting feature of the plots is the high degree of correlation between and among the various scans which is most evident in figures D2 and D3 from the plots along rows of a given column where the traces appear to be almost identical except for a small time lag that is almost imperceptible at the scale shown here. This high degree of correlation is, of course, not entirely unexpected since the scans represent the same cloud distribution sampled simultaneously at different locations. A further study to quantify the cross-band correlations using a variety of statistical approaches is being pursued elsewhere.

Acronyms

TRADOC	U.S. Army Training and Doctrine Command
NGIC	National Ground Intelligence Center
ARL	U. S. Army Research Laboratory
SLAD	Survivability Lethality Analyses Directorate
TTM	tools, techniques, and methods
MPTR	Multiple-Path Transmissometer Radiometer System
COMBIC	Combined Model for Battlefield Induced Contaminants
IR	infrared
ac	alternating current
dc	direct current
TRAC	TRADOC Analysis Center (TRADOC=Training and Doctrine Command)
SCIMITAR	Scene and Countermeasure Integration for Munition Interaction with Targets
CASTFOREM	Combined Arms and Support Task Force Evaluation Model

REPORT DOCUMENTATION PAGE

Form Approved
OMB No. 0704-0188

1. REPORT DATE *(DD-MM-YYYY)*	2. REPORT TYPE	3. DATES COVERED (From - To)
April 2003	Technical Report	

4. TITLE AND SUBTITLE

PILOT-81 VVA EXPERIMENT-Analysis of the Multi-Path Transmissometer-Radiometer Measurements

5a. CONTRACT NUMBER

5b. GRANT NUMBER

5c. PROGRAM ELEMENT NUMBER

6. AUTHOR(S)

R.A Sutherland and J.E. Butterfield

5d. PROJECT NUMBER

5e. TASK NUMBER

5f. WORK UNIT NUMBER

7. PERFORMING ORGANIZATION NAME(S) AND ADDRESS(ES)

U.S. Army Research Laboratory
Survivability/Lethality Analysis Directorate ATTN: AMSRL-SL-EM
Information & Electronic Protection Division
White Sands Missile Range, NM 88002-5513

8. PERFORMING ORGANIZATION REPORT NUMBER

ARL-TR-2953

9. SPONSORING/MONITORING AGENCY NAME(S) AND ADDRESS(ES)

U.S. Army Research Laboratory
2800 Powder Mill Road
Adelphi, MD 20783-1145

10. SPONSOR/MONITOR'S ACRONYM(S)

11. SPONSOR/MONITOR'S REPORT NUMBER(S)

ARL-TR-2953

12. DISTRIBUTION/AVAILABILITY STATEMENT

Approved for public release; distribution unlimited.

13. SUPPLEMENTARY NOTES

Key words: transmissometers, radiometers, obscurants, smokes, transmittance, contrast transmission, path radiance, aerosol emissivity, aerosol reflectivity, field measurements.

14. ABSTRACT

This report presents results and findings from the PILOT81 Emissive Sources Verification Experiments carried out at the Survivability/Lethality Analysis Directorate (SLAD), U.S. Army Research Laboratory Tower site at the White Sands Missile Range during February 1999. The experiments involved (near) simultaneous measurements of direct transmittance and normalized path emission/radiance sampled over three slightly diverging lines of sight through intervening obscurants comprised of either graphite flakes or brass powers of varying concentration levels. Specifically this report presents measurements of direct transmission and total radiance obtained over four spectral bands from the visible through far infrared using the SLAD Multiple Path Transmissometer-Radiometer (MPTR) system augmented with a conventional dual band infrared scanning imager. From the combined transmissometer and radiometer results we are able to determine both the multi-band transmittance and normalized path radiance, or "sky-to-ground" ratio, for cloud optical depths ranging from $\tau=0$ to about $\tau= 8$.

15. SUBJECT TERMS

Tranmissometers, radiometers, obscuranrts, emissivity, modeling, radiative transfer, field measurements

16. SECURITY CLASSIFICATION OF:			17. LIMITATION OF ABSTRACT	18. NUMBER OF PAGES	19a. NAME OF RESPONSIBLE PERSON
a. REPORT	b. ABSTRACT	c. THIS PAGE			R.A. Sutherland
U	U	U	SAR	60	19b. TELEPHONE NUMBER (*Include area code*) (505) 678-4520

Standard Form 298 (Rev. 8/98)
Prescribed by ANSI Std. Z39.18